EARLY EARTH

Large sulfur isotope fractionations associated with Neoarchean microbial sulfate reduction

Iadviga Zhelezinskaia,[1]* Alan J. Kaufman,[1] James Farquhar,[1] John Cliff[2]

The minor extent of sulfur isotope fractionation preserved in many Neoarchean sedimentary successions suggests that sulfate-reducing microorganisms played an insignificant role in ancient marine environments, despite evidence that these organisms evolved much earlier. We present bulk, microdrilled, and ion probe sulfur isotope data from carbonate-associated pyrite in the ~2.5-billion-year-old Batatal Formation of Brazil, revealing large mass-dependent fractionations (approaching 50 per mil) associated with microbial sulfate reduction, as well as consistently negative $\Delta^{33}S$ values (~ −2 per mil) indicative of atmospheric photochemical reactions. Persistent ^{33}S depletion through ~60 meters of shallow marine carbonate implies long-term stability of seawater sulfate abundance and isotope composition. In contrast, a negative $\Delta^{33}S$ excursion in lower Batatal strata indicates a response time of ~40,000 to 150,000 years, suggesting Neoarchean sulfate concentrations between ~1 and 10 μM.

The Archean Eon [4.0 to 2.5 billion years ago (Ga)] is generally characterized as a time in Earth history when oxygen was a trace constituent in the atmosphere (*1*) and oceanic sulfate abundance was lower than its present-day concentration by as much as a factor of 150 (*2*, *3*). Although sulfur isotope signatures in marine sedimentary rocks suggest that microbial sulfate reduction (MSR) was used as a metabolic strategy as far back as 3.5 Ga (*4*), overwhelming evidence for mass-independent sulfur isotope fractionations derived from atmospheric reactions (*5*) and preserved in Archean records argues against the prominence of contemporaneous MSR in the oceans (*6*–*9*). Iron speciation and trace metal abundances indicate a Neoarchean (2.5 to 2.8 Ga) role for MSR and sulfide production, implying euxinic (lacking oxygen but containing free hydrogen sulfide) conditions in some basins (*10*). Moreover, recent high-precision secondary ion mass spectrometry (SIMS) analyses of pyrite (*11*–*13*) and organic matter (*14*) in Archean successions reveal evidence of micrometer-scale mass-dependent sulfur isotope fractionation (MDF-S).

To further investigate the extent of MSR and the magnitude of MDF-S, we used multiple isotopic techniques to constrain temporal and spatial changes in sulfur and carbon cycling in a Neoarchean sedimentary succession from Brazil (*15*). We focused on samples from the ~2.5 Ga Batatal Formation (fig. S1) collected from an exploration drill core (GDR-117 provided by AngloGold Ashanti) intersecting ~180 m of strata (Fig. 1). The shallow marine Batatal platform, which is composed of two shale-rich intervals above and below a stromatolitic carbonate, is considered to be a time equivalent of once-contiguous deep-water slope successions in the Hamersley basin of Western Australia and the Transvaal basin of South Africa (*16*) (fig. S2). This geographically and spatially discrete sedimentary unit thus provides a unique opportunity to examine similarities and differences in sediment geochemistry across the terminal Neoarchean world.

Distal shale and proximal carbonate facies of the Batatal Formation reveal large sulfur isotope variations (Fig. 1). Pyrite in carbonate (and to a lesser degree in carbonaceous shale) is depleted in ^{34}S and ^{33}S relative to black shale facies. In microdrilled and bulk carbonate-associated pyrite (CAP), $\delta^{34}S$ values (*17*) were as low as −30 per mil (‰) and −14‰, respectively, and both phases were found to have consistently negative $\Delta^{33}S$ values (*18*). In contrast, samples from shale-rich facies are relatively more enriched in both ^{34}S and ^{33}S, depending on carbonate content (fig. S4). SIMS pyrite analyses in a subset of five carbonate samples were conducted to examine the extent of micrometer-scale sulfur isotopic variation within grains and across textural boundaries (fig. S6). Although the $\Delta^{33}S$ values determined by SIMS mirror those of bulk and microdrilled samples, the ion probe $\delta^{34}S$ measurements reveal even greater degrees of ^{34}S depletion, with pyrite $\delta^{34}S$ values as low as −38‰. Notably, SIMS analyses yielding the most negative $\delta^{34}S$ values also have constant $\Delta^{33}S$ (Fig. 2A). Although some macroscopic pyrite samples drilled in the upper Batatal carbonaceous shale have negative $\Delta^{33}S$ values and $\delta^{34}S$ signatures as low as −13.6‰, we did not study these samples by the SIMS technique and thus do not know whether these pyrite grains preserve the fine-scale variability and extreme ^{33}S and ^{34}S depletions seen in the carbonate samples. The SIMS pyrite data from carbonate samples in the interval between 1261 and 1272 m form arrays indicating similar levels of ^{33}S depletion (~ −2‰), whereas the array of measurements from the sample 36 m lower in the core (1308 m) defines a $\Delta^{33}S$ floor at −3‰.

The SIMS determinations of $\Delta^{36}S/\Delta^{33}S$ for the Batatal CAP grains are consistent with those of bulk and microdrilled analyses (Fig. 2B), and most fall in the range of previously published Neoarchean data (*5*, *12*) characterized by a $\Delta^{36}S/\Delta^{33}S$ slope of ~ −1. In some cases (e.g., samples 1308.08, 1266.72, and 1261.90), however, coupled values lie below the reference array, indicating greater depletion in ^{36}S abundances (fig. S8). We attribute the additional ^{36}S depletion in CAP to a metabolic response of MSR at the time the Batatal carbonates were deposited (see fig. S8). Experiments on modern sulfate reducers (*19*) show that variations within and relationships between multiple sulfur isotopes are produced by bacteria grown under different conditions, likely reflecting the differential transport of sulfate into and out of the cells. On the other hand, Rayleigh distillation (*20*) is also known to produce variations in $\Delta^{36}S$, but this process also generates large variability in $\delta^{34}S$ that is not observed in the data from this study (*15*) (fig. S9).

Carbon isotope measurements of shale and carbonate in the Batatal Formation reveal a pronounced difference between deep- and shallow-water facies. The magnitude of carbon isotope fractionation between carbonate carbon and organic carbon ($\Delta^{13}C_{carb-org}$) in shale and carbonate facies is remarkably constant, with values generally ranging between 15 and 20‰ (Fig. 1). This range of fractionation is much smaller than that measured in the broadly equivalent units from Western Australia and South Africa [~30‰ (*21*, *22*)] (Fig. 1 and fig. S10). Reduced fractionation is unlikely the result of metamorphism but may be biologically mediated in the deep ocean environment. Sedimentological and petrographic observations coupled with a comparison of modern shallow marine environments suggest that the reduced fractionation may be the result of carbon limitation in an evaporitic setting (*15*) where oceanic sulfate was potentially concentrated.

Sulfur isotope compositions of CAP also differ between this study and prior research on temporally equivalent Neoarchean successions in Western Australia (*21*) and South Africa (*23*). In those reports, $\delta^{34}S$ values in mixed shale and carbonate facies that accumulated in continental slope settings fell to a nadir of −10‰ in bulk rock measurements and down to −21‰ for SIMS analysis (*12*). New SIMS results from the Batatal Formation reveal even more negative $\delta^{34}S$ pyrite values as low as −38‰ (Fig. 2). Coupled with the estimated range of terminal Neoarchean seawater sulfate compositions (+6 to +15‰) [compare with (*3*, *24*)], this observation suggests that MDF-S values were as much as 40 to 50‰. The magnitude of this fractionation is considerable, even in comparison with those recorded in modern environments (*6*).

[1]Department of Geology and Earth System Science Interdisciplinary Center, University of Maryland, College Park, MD 20742, USA. [2]Centre for Microscopy Characterization and Analysis, ARC Centre of Excellence for Core to Crust Fluid Systems, University of Western Australia, Crawley, WA 6009, Australia.
*Corresponding author. E-mail: zhelezka@umd.edu

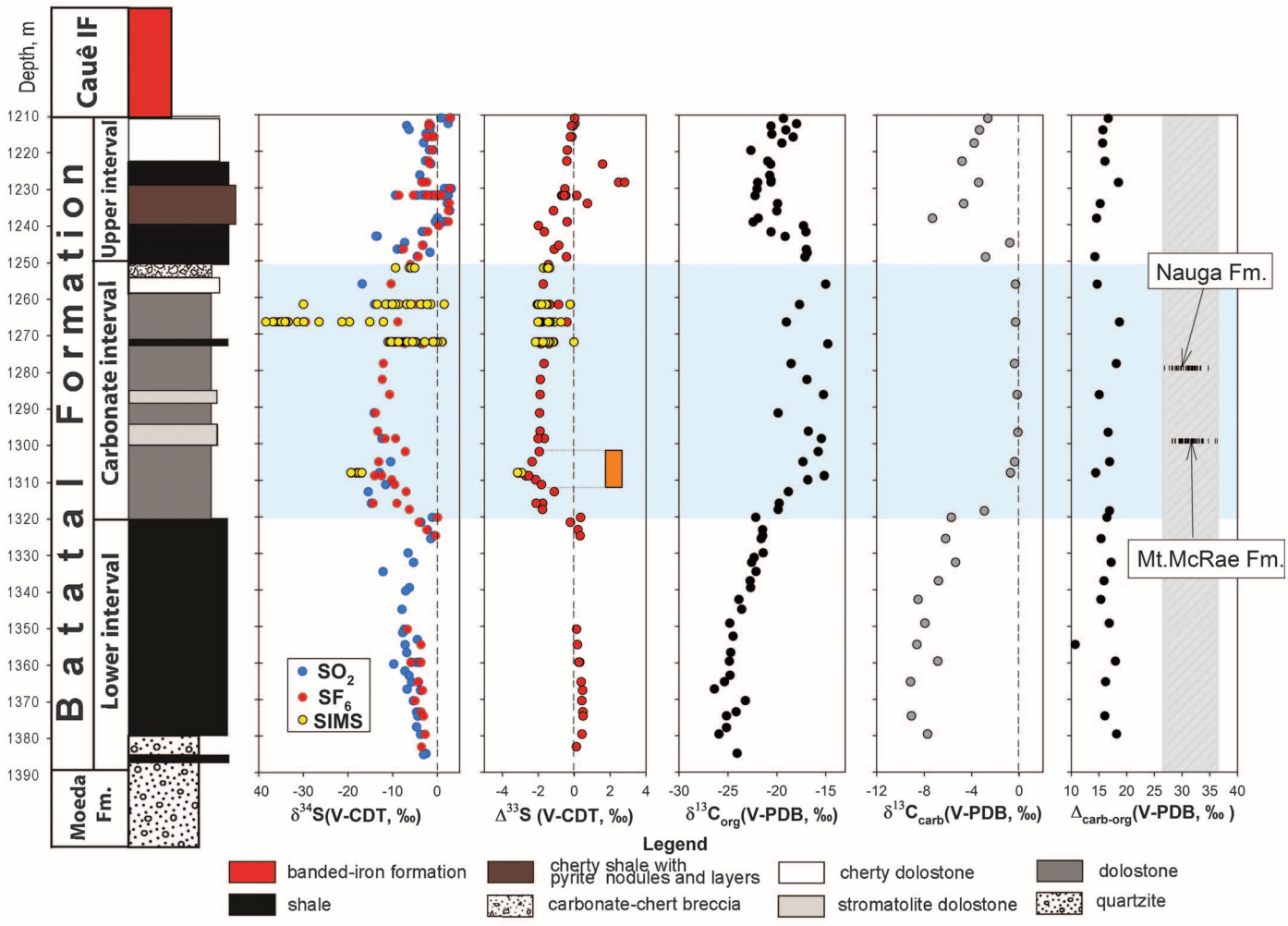

Fig. 1. High-resolution time-series sulfur and carbon isotopic data from ~2.5 Ga Batatal Formation in Brazil. The most negative $\delta^{34}S$ and $\Delta^{33}S$ values are recorded exclusively in the carbonate interval. Although the carbonates record shows large variations in $\delta^{13}C$ between shallow- and deep-water facies, the magnitude of carbon isotope fractionation between coexisting organic and inorganic phases ($\Delta_{carb-org}$) is relatively constant and unusually small. Shaded area represents extent of carbon isotope fractionation in Neoarchean formations from Western Australia [Mt. McRae Shale Formation, from (*21*)] and South Africa [Nauga Formation, from (*22*)].

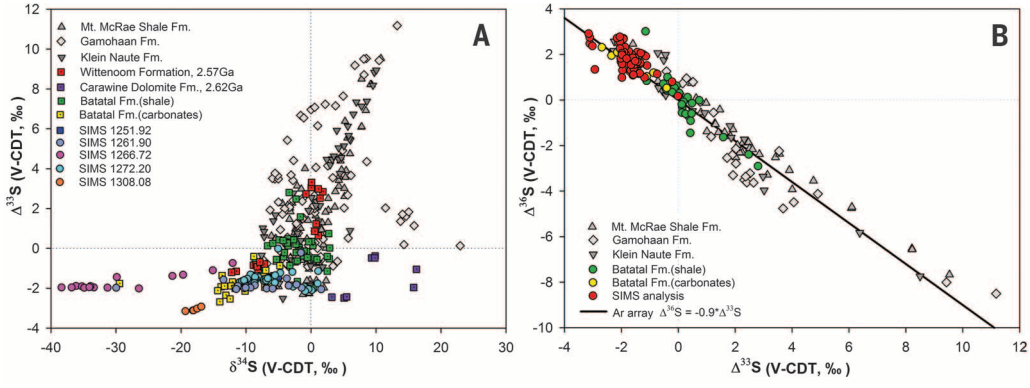

Fig. 2. Sulfur isotope data for the Batatal Formation in the context of published Neoarchean measurements. (**A**) Cross-plot of $\Delta^{33}S$ versus $\delta^{34}S$ values of pyrites from Neoarchean successions from South Africa (*20*, *22*) and Western Australia (*20*, *23*, *31*) as well as bulk and SIMS measurements from Batatal shale and carbonate samples. The bulk Batatal data show large sulfur isotope fractionation in CAP attributed to microbial sulfate reduction; the SIMS analyses reveal two different floors of $\Delta^{33}S$ values at negative $\delta^{34}S$. (**B**) Cross-plot of $\Delta^{36}S$ versus $\Delta^{33}S$ values of various Neoarchean successions (*20*, *22*); note that Batatal carbonates have consistently negative $\Delta^{33}S$ and consistently positive $\Delta^{36}S$ values, likely defining end-member compositions on the Archean array.

Habicht *et al.* (*2*) argued that large fractionations would not be preserved in typical shale facies unless pore water sulfate concentrations were higher than 200 μM (for comparison, modern seawater SO_4^{2-} is 28 mM). This threshold now appears to be an upper limit, as recent observations of modern meromictic lakes (*25*, *26*) with SO_4^{2-} as low as 25 to 100 μM indicate that isotopic fractionation of more than 20‰ is

possible. The discrepancy between microscale sulfur isotope measurements that reveal evidence for strongly negative $\delta^{34}S$ values [e.g., (*13, 14*)] and bulk measurements that fail to yield a clear indication of strongly negative $\delta^{34}S$ signatures may reflect SO_4^{2-} transport limitation (closed or partially closed) in Archean sediments. The strongly negative and variable $\delta^{34}S$ with constant $\Delta^{33}S$ and variable $\Delta^{36}S$ at the micrometer scale supports this interpretation applied to the Batatal depositional environment; this further provides a link between Batatal sediment pore fluids and overlying seawater sulfate. The greater ^{34}S depletion in the microscale analyses relative to bulk measurements also implies mass-dependent redistribution of sulfur isotopes by MSR within the sediments. However, the average negative $\delta^{34}S$ pyrite values (~ −10‰) preserved in bulk samples relative to the inferred positive $\delta^{34}S$ composition of coeval seawater SO_4^{2-} imply that the system was not completely closed [the proportional fraction of sulfate reduced would be ~0.5 to 0.7, assuming a starting sulfate composition of 15‰ and a fractionation of 50‰ (*15*)].

The large sulfur isotope fractionations observed here imply that MSR did not deplete and fractionate residual pore water sulfate to a large enough extent that transport limitation controlled the expression of isotopic compositions. Following recent suggestions (*27*) that the availability of electron donors, cell-specific growth rates, and sulfur isotope fractionation are interdependent, we interpret the production and preservation of sulfide with strongly negative $\delta^{34}S$ values to reflect a lower proportion of electron donors (i.e., organic matter or H_2) relative to sulfate ([e^- donor]/[SO_4^{2-}]) in the Batatal shallow marine carbonate-rich environment relative to those found in typical Archean shales. Indeed, organic carbon contents in the Brazilian sediments are much lower than contemporary deep-water facies from Western Australia and South Africa. We further suggest that Batatal CAPs derive their sulfur predominantly from sulfate reduction, rather than from an atmospherically derived source carrying positive $\delta^{34}S$ and $\Delta^{33}S$ compositions. Our observations of the shallow and potentially evaporitic Batatal carbonate are in agreement with model predictions (*28*) suggesting greater contributions of atmospherically derived elemental sulfur (with positive $\Delta^{33}S$) to distal environments, whereas sulfate sourced from the atmosphere (with negative $\Delta^{33}S$) and from continental weathering was concentrated in proximal settings.

A notable feature of the SIMS analyses of samples at 1266.72, 1261.90, and 1272.20 m depth is the almost constant $\Delta^{33}S$ [average −1.7 ± 1.02‰ (2σ)] for the most highly fractionated (most negative $\delta^{34}S$ values) pyrite grains (Fig. 2). This array suggests variations in MDF-S associated with MSR from a starting sulfate pool with a constant negative $\Delta^{33}S$. The relatively constant $\Delta^{33}S$ over nearly 60 m of the Batatal Formation carbonate is interpreted to reflect a long-term stability [~0.4 to 1.5 million years, based on a carbonate accumulation rate of 40 to 150 m per million years (*29*)] in the $\Delta^{33}S$ composition of sulfate supplied to the shallow marine environment (i.e., the proportion of atmospheric and nonatmospheric sulfate was stable over the depositional interval).

The negative shift in $\Delta^{33}S$ values of samples between core depths of 1302 to 1308 m, however, suggests a secular change in the isotopic composition of oceanic sulfate. The amount of time necessary for shallow marine carbonate accumulation of ~6 m is relatively short (40,000 to 150,000 years) but is still sufficiently long to suggest that $\Delta^{33}S$ was well mixed in the oceans. According to our calculations, the residence time of sulfate was lower than the response time by a factor of 2. Thus, order-of-magnitude constraints can be placed on oceanic sulfate concentrations of 10^{-5} to 10^{-6} mol/liter assuming only volcanic fluxes (~10^{11} mol/year), or higher if weathering fluxes are also included (*15*). Our Neoarchean sulfate concentration estimate is consistent with previous assessments (*2*, *3*).

The connection between pyrite with negative $\Delta^{33}S$ and oceanic sulfate implies that at the time the Batatal Formation was deposited, the source of oceanic sulfate had a predominantly negative $\Delta^{33}S$ composition. If correct, the negative oceanic $\Delta^{33}S$ signature indicates that the atmospheric source of sulfate dominated over that of elemental sulfur, and that sources of sulfate from the oxidation of sedimentary sulfides with positive $\Delta^{33}S$ (*10*) were negligible. This conclusion implies either that late Neoarchean oxidative weathering occurred at low levels, or that weathering fluxes of sulfate were episodic and somehow were not captured by the Batatal CAPs.

Evaluated in the context of the long-term Archean bias toward positive pyrite $\Delta^{33}S$ compositions (*30*) (fig. S11), our analyses suggest that MSR was an important sink for sulfate with negative $\Delta^{33}S$ in the Neoarchean ocean. Support for this view comes from analyses of CAP with negative $\Delta^{33}S$ in slightly older carbonate-rich Neoarchean strata of Western Australia (Fig. 2A) (*24*, *31*), including the Carawine Dolomite, which contains textural evidence for shallow marine evaporitic conditions (*32*), as inferred from the sedimentology of the Batatal carbonates. Given the low concentration of CAP in Batatal bulk samples and relative abundances of carbonate and shale in Neoarchean successions (*33*), however, we estimate that carbonates could represent only about 1% of the negative $\Delta^{33}S$ sink necessary to balance the sulfur cycle (*15*). Other chemical inventories in the oceans, including basinal banded iron formations (*30*) and abyssal hydrothermal volcanogenic massive sulfide deposits (*3*), must therefore have been the dominant sinks for atmospherically derived sulfate with negative $\Delta^{33}S$ compositions.

REFERENCES AND NOTES

1. A. A. Pavlov, J. F. Kasting, *Astrobiology* **2**, 27–41 (2002).
2. K. S. Habicht, M. Gade, B. Thamdrup, P. Berg, D. E. Canfield, *Science* **298**, 2372–2374 (2002).
3. J. W. Jamieson, B. A. Wing, J. Farquhar, M. D. Hannington, *Nat. Geosci.* **6**, 61–64 (2013).
4. Y. Shen, J. Farquhar, A. Masterson, A. J. Kaufman, R. Buick, *Earth Planet. Sci. Lett.* **279**, 383–391 (2009).
5. J. Farquhar, J. Savarino, S. Airieau, M. H. Thiemens, *J. Geophys. Res.* **106**, 32829–32839 (2001).
6. D. E. Canfield, *Am. J. Sci.* **304**, 839–861 (2004).
7. D. T. Johnston, *Earth Sci. Rev.* **106**, 161–183 (2011).
8. I. Halevy, D. T. Johnston, D. P. Schrag, *Science* **329**, 204–207 (2010).
9. C. T. Reinhard, N. J. Planavsky, T. W. Lyons, *Nature* **497**, 100–103 (2013).
10. C. T. Reinhard, R. Raiswell, C. Scott, A. D. Anbar, T. W. Lyons, *Science* **326**, 713–716 (2009).
11. B. S. Kamber, M. J. Whitehouse, *Geobiology* **5**, 5–17 (2007).
12. J. Farquhar *et al.*, *Proc. Natl. Acad. Sci. U.S.A.* **110**, 17638–17643 (2013).
13. D. Wacey, M. R. Kilburn, M. Saunders, J. Cliff, M. D. Brasier, *Nat. Geosci.* **4**, 698–702 (2011).
14. T. R. Bontognali *et al.*, *Proc. Natl. Acad. Sci. U.S.A.* **109**, 15146–15151 (2012).
15. See supplementary materials on *Science* Online.
16. E. S. Cheney, *Precambrian Res.* **79**, 3–24 (1996).
17. Sulfur has four stable isotopes: two more abundant (^{32}S and ^{34}S) and two rare (^{33}S and ^{36}S) isotopes. Sulfur isotope composition of materials is reported as $\delta^xS = 1000 \times [(^xS/^{32}S)_{sample}/(^xS/^{32}S)_{standard} - 1]$, where x is 33, 34, or 36.
18. The deviation from the mass-dependent relationships is calculated by the following equations: $\Delta^{33}S = \delta^{33}S - 1000 \times [(\delta^{34}S/1000 + 1)^{0.515} - 1]$ and $\Delta^{36}S = \delta^{36}S - 1000 \times [(\delta^{34}S/1000 + 1)^{1.90} - 1]$.
19. D. T. Johnston, J. Farquhar, D. E. Canfield, *Geochim. Cosmochim. Acta* **71**, 3929–3947 (2007).
20. S. Ono, B. Wing, D. Johnston, J. Farquhar, D. Rumble, *Geochim. Cosmochim. Acta* **70**, 2238–2252 (2006).
21. A. J. Kaufman *et al.*, *Science* **317**, 1900–1903 (2007).
22. W. W. Fischer *et al.*, *Precambrian Res.* **169**, 15–27 (2009).
23. S. Ono, A. J. Kaufman, J. Farquhar, D. Y. Sumner, N. J. Beukes, *Precambrian Res.* **169**, 58–67 (2009).
24. S. Ono *et al.*, *Earth Planet. Sci. Lett.* **213**, 15–30 (2003).
25. G. Paris *et al.*, *Mineral. Mag.* **76**, 2204 (2012).
26. M. L. Gomes, M. T. Hurtgen, *Geology* **41**, 663–666 (2013).
27. W. D. Leavitt, I. Halevy, A. S. Bradley, D. T. Johnston, *Proc. Natl. Acad. Sci. U.S.A.* **110**, 11244–11249 (2013).
28. I. Halevy, *Proc. Natl. Acad. Sci. U.S.A.* **110**, 17644–17649 (2013).
29. W. Altermann, D. R. Nelson, *Sediment. Geol.* **120**, 225–256 (1998).
30. J. Farquhar, B. A. Wing, *Earth Planet. Sci. Lett.* **213**, 1–13 (2003).
31. M. A. Partridge, S. D. Golding, K. A. Baublys, E. Young, *Earth Planet. Sci. Lett.* **272**, 41–49 (2008).
32. B. M. Simonson, K. A. Schubel, S. W. Hassler, *Precambrian Res.* **60**, 287–335 (1993).
33. K. C. Condie, D. J. Des Marais, D. Abbott, *Precambrian Res.* **106**, 239–260 (2001).

ACKNOWLEDGMENTS

We thank C. Noce, N. Geboy, and A. Shrestha, as well as the facilities and the scientific and technical assistance of the Australian Microscopy and Microanalysis Research Facility at the Centre for Microscopy, Characterization and Analysis at the University of Western Australia, a facility funded by the University, State, and Commonwealth governments. Supported by the Fulbright Program (grantee ID 15110620, I.Z.), NASA Astrobiology Institute grant NNA09DA81A (J.F.), and NSF Frontiers of Earth Surface Dynamics program grant 432129 (A.J.K.). All data are provided in the supplementary materials.

SUPPLEMENTARY MATERIALS

www.sciencemag.org/content/346/6210/742/suppl/DC1
Materials and Methods
Supplementary Text
Figs. S1 to S12
Tables S1 and S2
References (*34*–*72*)

19 May 2014; accepted 12 September 2014
10.1126/science.1256211

www.sciencemag.org/content/346/6210/742/suppl/DC1

Supplementary Materials for

Large sulfur isotope fractionations associated with Neoarchean microbial sulfate reduction

Iadviga Zhelezinskaia,* Alan J. Kaufman, James Farquhar, John Cliff

*Corresponding author. E-mail: zhelezka@umd.edu

Published 7 November 2014, *Science* **346**, 742 (2014)
DOI: 10.1126/science.1256211

This PDF file includes:

Other supplementary material for this manuscript includes the following:

Materials

Geological setting of the GDR-117 core

The Batatal Formation is a part of the upper Caraça Group of the Minas Supergroup in Brazil (Fig. S1). The age of the Batatal Formation is currently constrained by a U-Pb detrital zircon minimum age of 2.58 Gyr in the underlying but conformable Moeda Formation (*34*) and a Pb-Pb carbonate age of 2.42 Gyr in the overlying Gandarela Formation (*35*; see Fig. S2). The Minas Supergroup sedimentary succession has been subjected to two tectonic events, including the Transamazonian (ca. 2.2-2.0 Gyr) and Brasiliano (ca. 0.6-0.5 Gyr) orogenies (*36*) and has a cumulative degree of metamorphism reflecting lower greenschist facies (*37, 38*).

The Batatal Formation is widespread, but is rarely preserved in outcrops; where it does occur on the surface it is highly weathered. Our samples were collected from AngloGold Ashanti core GDR-117 drilled near Belo Horizonte. The Batatal strata, consisting of three distinct members – including lower shale, a middle siliceous carbonate, and an upper interval of mixed shale, carbonate, and chert – were intersected at depths between 1210 and 1390 meters.

The lower 65 m of the Batatal Fm. (Figs. S2, S3, S4) consists of grey to black laminated shale, which contains variable amounts of carbonate (16.88±19.47%) associated with dolomitic turbidites or the production of siderite in the distal platform environment (Table S1). Total organic carbon (TOC) contents in samples from the lower shale member are generally less than 1.0% (0.67±0.27%, 1σ). The carbon isotopic composition of TOC rises up section from -27 to -23‰, which is coincident with that of carbonate carbon that rises from -9 to -6‰. Oxygen isotope compositions of carbonate in the lower member samples are variable, ranging from -14 to -17‰. Pyrite in homogeneous bulk samples from this interval is low in abundance (0.002±0.002%, 1σ), although it occasionally occurs as large diagenetic nodules up to two cm in diameter and as irregular veins associated with chert.

The grey silicified stromatolitic and laminated dolomite member is 67 m thick (Figs. S2, S3, S4) and is brecciated, heavily silicified, and karstified at its top. The unit contains occasional shale stringers where TOC abundances are higher, but is generally lacking in organic matter (0.41±0.63%, 1σ); carbon isotopic compositions of TOC are enriched in ^{13}C relative to typical Neoarchean organic matter, with $\delta^{13}C$ values ranging from -15 to -20‰. In contrast, the carbonate fraction (78.90±8.2%) of samples in this interval mostly has $\delta^{13}C$ values very near to 0‰. Pyrite in the carbonate member is most often found associated with organic carbon and silica along laminations or as 1) isolated 20 to 200 μm euhedral grains, 2) irregular aggregates of grains up to 500 μm in diameter, and 3) partial replacement of chert patches or veins (Figs. S3, S5, S6). The average abundance of carbonate associated pyrite sulfur in our samples from this interval is 0.020±0.026% (1σ).

The uppermost member, which disconformably overlies the thick carbonate, includes 38 m of mixed carbonate and carbonaceous, siliceous, or pyritic grey to black shale, marl, and chert (Fig S3, S4). Overall this interval is enriched in silica in the form of veins, irregularly-shaped segregations, laminations, and beds, and the unit conformably

transitions into the overlying Cauê Iron Formation. In most samples pyrite is finely disseminated with a grain size of 30-50 μm , but 100 μm euhedra are concentrated along some laminations, and even larger aggregates and nodules (up to 5 cm) are common in the pyritic interval between 1230 and 1240 m. Average sulfur abundance in samples from this interval is 0.585±1.570% (1σ). Carbonate contents in the upper member vary widely (49.01±30.04%, 1σ) but are clearly lower at the base of the unit and rise up section; the carbon isotope compositions of samples from this member range from -7 to near 0‰, but have a narrow range of $\delta^{18}O$ values around -14‰. TOC abundance in the upper interval is higher than in underlying units (2.42±3.38%) and is significant in the pyritic interval with contents as high as 14%.

In light of these sedimentological and geochemical observations, it appears that the Batatal Formation initially accumulated over coarse Moeda sandstones and conglomerates during rapid transgression. After maximal flooding, sea level gradually fell represented by the shale to carbonate transition in the lower two members. The presence of stromatolitic, laminated, and massive dolomites in the middle carbonate member suggests accumulation in subtidal to peritidal environments, with the likelihood of episodically evaporitic conditions suggested by the ubiquitous presence of chert in the carbonate samples. Karstification, brecciation, and silicification at the top of the carbonate member indicate exposure and stratigraphic truncation of the platform. Renewed sedimentation of mixed carbonate and shale with increasing silica contents leading into the overlying Cauê Iron Formation indicates an overall transgressive cycle with accumulation in slope to basinal facies.

The lithological transitions (carbonate to pyritic shale to iron-formation) preserved in the Batatal succession coupled with available age constraints suggests that these strata are likely correlative with terminal Neoarchean units in Western Australia (Mt. McRae shale and Brockman Iron Formation) and South Africa (Gamohaan/Klein Naute and Kuruman Iron Formation)(Fig. S2). Scientific cores drilled through these successions, which accumulated in a once contiguous basin (*15*), have been the focus of a number of recent geochemical investigations. The Brazilian succession was likely deposited in a separate basin, and thus provides an important contrast in which to compare globally-distributed events.

Methods

Isotopic notation

Isotopic composition of any material is usually described using delta (δ) notation. For sulfur isotopic systematics:

$$\delta\,{}^{x}S = \left[\frac{\left({}^{x}S/{}^{32}S\right)_{sample}}{\left({}^{x}S/{}^{32}S\right)_{std}} - 1\right] \times 1000$$

Where ^{32}S represents the most abundant stable isotope and ^{x}S represents sulfur isotopes with masses 33, 34, and 36 amu. The standard (std) used for normalization is IAEA certified Vienna-Canyon Diablo Troilite (V-CDT). The capital delta (Δ) notation is

used to quantify magnitudes of sulfur isotope deviation from the mass-dependent reference fractionation line. For the rare isotopes ^{33}S and ^{36}S:

$$\Delta^{33}S = \delta^{33}S - \left[\left(1 + \frac{\delta^{34}S}{1000}\right)^{0.515} - 1\right] \times 1000$$

$$\Delta^{36}S = \delta^{36}S - \left[\left(1 + \frac{\delta^{34}S}{1000}\right)^{1.90} - 1\right] \times 1000$$

For carbon and oxygen isotope systematics:

$$\delta^{13}C = \left[\frac{\left(^{13}C/^{12}C\right)_{sample}}{\left(^{13}C/^{12}C\right)_{std}} - 1\right] \times 1000 \qquad \delta^{18}O = \left[\frac{\left(^{18}O/^{16}O\right)_{sample}}{\left(^{18}O/^{16}O\right)_{std}} - 1\right] \times 1000$$

The standard for carbon and oxygen isotopes in carbonates and for carbon isotopes in organic carbon is Vienna Pee Dee Belemnite (V-PDB).

Sulfur bulk rock analyses

All samples from the core GDR-117 were powdered by hand using a ceramic mortar and pestle. In addition, macroscopic pyrite grains were sampled with a drill press and a 0.8 mm diameter fluted carbide bit.

For bulk analysis, carbonates were pre-acidified with 3M HCl and the solid residue was then reacted with a gently boiled solution of 5M HCl and Cr(II) solution at 80°C temperature for 3.5 hours to release hydrogen sulfide that was carried by flowing nitrogen gas. The hydrogen sulfide was passed through a bubbler filled with deionized water and then trapped in 15 ml of a 0.03M silver nitrate ($AgNO_3$) solution, which resulted in precipitation of silver sulfide (Ag_2S). The Ag_2S was aged in the dark for one week at room temperature and then filtered, washed with 1M NH_4OH and ultrapure Milli-Q water, and dried at 50°C overnight.

Sulfur isotope ratios were determined using either an Elementar Isoprime continuous flow isotope ratio mass spectrometer (SO_2) or a ThermoFinnigan MAT 253 (SF_6) dual inlet isotope ratio mass spectrometer. Both instruments are housed in the Stable Isotope Laboratory in the University of Maryland Geology Department.

Continuous flow measurements: For SO_2 measurements V_2O_5 was mixed with the Ag_2S samples (100±10 μg) to enhance combustion to SO_2. The tin cups were sequentially dropped with a pulsed O_2 purge of 12 ml into a catalytic combustion of a Eurovector elemental analyzer furnace operating at 1030℃. The frosted quartz reaction tube was packed with high purity reduced copper wire for quantitative oxidation and O_2 resorption. Water was removed from the combustion products with a 10-cm magnesium perchlorate column, and the SO_2 was separated from other gases with a 0.8-m PTFE GC column packed with Porapak 50–80 mesh heated to 115◦C. The effluent from the elemental analysis (EA) was introduced in a flow of He (80–120 mL/min) to the Elementar Isoprime IRMS through a SGE splitter valve that controls the variable open split. Timed

pulses of SO_2 reference gas (Air Products 99.9% purity, ~3 nA) were introduced at the beginning of the run using an injector connected to the IRMS with a fixed open ratio split. The isotope ratios of reference and sample peaks were determined by monitoring ion beam intensities relative to background values. The cycle time for these analyses was 210 seconds with reference gas injection as a 30-second pulse beginning at 20 seconds. Sample SO_2 pulses begin at 110 seconds and return to baseline values between 150 and 180 seconds, depending on sample size and column conditions. Sulfur isotope ratios were determined by comparing integrated peak areas of m/z 66 and 64 for the reference and sample SO_2 pulses, relative to the baseline that is approximately 1×10^{-11}A. The background height was established from the left limit of the sample SO_2 peak. Isotopic results are expressed in the delta notation as per mil (‰) deviations from the Vienna Canyon Diablo Troilite (V-CDT) standard. Two NBS 127 barite standards and two IAEA-1 silver sulfide standards were measured between each set of 10 samples and uncertainties for each analytical session based on these standard analyses were determined to be better than 0.3‰ (1σ).

Dual inlet measurements: For isotopic measurements of SF_6 two to three mg of AgS_2 (either as sample or IAEA standard) was placed in aluminum foil packets and then transferred to evacuated Ni reaction vessels. The AgS_2 was reacted with an atmosphere of F_2 gas at 250°C at a pressure of about 3 Torr overnight to convert Ag_2S to gaseous SF_6. The SF_6 was then purified using several steps of cryogenic separation, passivation, and gas-chromatographic purification. A ThermoFinnigan MAT 253 was used to measure ratios of masses 127, 128, 129, and 131 ($^{32}SF_5^+$, $^{33}SF_5^+$, $^{34}SF_5^+$, and $^{36}SF_5^+$, respectively). The ThermoFinnigan MAT 253 measurements have estimated uncertainties of 0.14, 0.008, and 0.2 (1σ) for $\delta^{34}S$, $\Delta^{33}S$, and $\Delta^{36}S$, respectively. The uncertainties are estimated on the basis of long-term reproducibility of standard materials.

Sulfur SIMS analyses

Five samples from the carbonate member with significantly negative $\Delta^{33}S$ values based on bulk analyses were measured by a SIMS technique at the University of Western Australia (see Table S2 and Fig. S6): 1251.92 (quartz – carbonate breccia), 1261.90 (massive dolostone), 1266.72 (massive dolostone), 1272.20 (shale inter-bedding the carbonate interval), and 1308.08 (thin laminated carbonate). Sulfur isotope ratios were determined using a Cameca IMS 1280 ion microprobe at the Centre for Microscopy, Characterization and Analysis (CMCA) at the University of Western Australia. In all cases ^{32}S, ^{33}S, and ^{34}S and ^{36}S were measured simultaneously in multi-collection mode. In all cases NMR regulation was used and ^{32}S, ^{33}S, and ^{34}S were measured using Faraday cup detectors (FC). In contrast, ^{36}S was measured using an electron multiplier (EM). Count rates for ^{32}S were on the order of 10^9 cps while for the minor ^{36}S they were on the order of 10^5 cps (see Table S2). The in house standard SON-3 was used to correct for instrumental mass fractionation and to calibrate unknowns against V-CDT. Analysis spot sizes were ~ 25 μm × 25 μm. Unknowns were bracketed with standards of known composition. Temporal variations of $\delta^{34}S$, $\Delta^{33}S$ and $\Delta^{36}S$ in standards that bracketed the unknowns are plotted in Figure S6. Average external precision (1σ) for standard analyses

were $\delta^{33}S$ =0.05‰, $\delta^{34}S$ =0.08‰, $\delta^{36}S$ =0.19‰, $\Delta^{33}S$=0.02‰, and $\Delta^{36}S$ = 0.20‰. For more details about analytical conditions and data processing see reference (*12*).

Carbon and oxygen isotope analyses

Carbonates: Carbonate C and O isotopes were measured rapidly by continuous flow-isotope ratio mass spectrometry in the University of Maryland Paleoclimate CoLaboratory using a refined method for the analysis and correction of carbon ($\delta^{13}C$) and oxygen ($\delta^{18}O$) isotopic composition of 100 μg carbonate samples (*39*). Up to 180 samples loaded into 3.7 mL Labco Exetainer vials and sealed with Labco septa were flushed with 99.999% helium and manually acidified at 60℃. The carbon dioxide analyte gas was isolated via gas chromatography, and water was removed using a Nafion trap prior to admission into an Elementar Isoprime stable isotope mass spectrometer fitted with a continuous flow interface. Data were corrected via automated Matlab scripting on the Vienna PeeDee Belemnite and LSVEC Lithium Carbonate (VPDB-LSVEC) scale (*40*) using periodic in-run measurement of international reference carbonate materials and/or in-house standard carbonates, from which empirical corrections for signal amplitude, sequential drift, and one or two-point mean corrections were applied. Precision for both isotopes is routinely better than 0.1‰ (1σ). Including acidification, flush fill, reaction and analysis, true throughput exclusive of correcting standards is 2–3 samples/hour, or up to 144 samples over a 40-hour analytical session.

Organic matter: Measurements of organic carbon abundance and carbon isotope composition with the Eurovector elemental analyzer and Elementar Isoprime continuous flow isotope ratio mass spectrometer were similar to those of sulfur, except that the reaction column was packed with chromium oxide and silvered cobaltous/cobaltic oxide and heated to 1040°C and the analyte also flows through a second column at 1040°C packed with high purity reduced copper wire for quantitative reduction of NO_2 and N_2O and O_2 resorption. The CO_2 was separated from other gases with a 3-m stainless steel GC column packed with Porapak-Q heated to 60◦C. Timed pulses of CO_2 reference gas (Airgas 99.999% purity, ~6 nA) were introduced at the beginning of the run using an injector connected to the IRMS with a fixed open ratio split. The isotope ratios of reference and sample peaks were determined by monitoring ion beam intensities relative to background values. The cycle time for these analyses was 430 s with reference gas injection as two a 30-s pulse beginning at 15 and 60 s. Sample CO_2 peaks begin at 200 s and return to baseline around 240 s. Carbon isotope ratios were determined by comparing integrated peak areas of m/z 45 and 44 for the reference and sample CO_2 pulses, relative to the baseline that is approximately 2×10^{-11}A. The background height was established from the left limit of the sample CO_2 peak. Isotopic results are expressed in the delta notation as per mil (‰) deviations from the Vienna Pee Dee Belemnite (V-PDB) standard. Two urea standards were measured between each set of 10 samples and uncertainties for each analytical session based on these standard analyses were determined to be better than 0.1‰.

Supplementary Text

Rayleigh distillation

Observation of $\Delta^{36}S/\Delta^{33}S$ relationships from SIMS analyses of carbonate associated pyrite (Fig. S8) that differs from the Archean reference array (*23*) may reflect either a Rayleigh distillation process in a closed system (*19*) or microbial sulfate reduction (*18*). To test between these alternatives we used the Rayleigh equation,

$$R = R_0 \cdot f^{(\alpha-1)},$$

to calculate the isotopic composition of residual sulfate, and

$$R_p = R_0 \cdot (1-f^{\alpha}))/(1-f),$$

to calculate the isotopic composition of pooled product, where R_0 is the initial isotopic composition of sulfate, R is the remaining isotopic composition of sulfate, f is fraction of remaining sulfate, α is the fractionation factor, and R_p is the isotopic composition of instantaneous product (as pyrite). Using this equation, we calculated $\delta^{34}S$, $\Delta^{33}S$ and $\Delta^{36}S$ compositions for the range of fractionation observed in the sample from 1308 m depth where isotope relationships are most pronounced. The calculations demonstrate large fractionations for ^{34}S that are not apparent in the sample. This suggests that a Rayleigh process does not provide a good explanation for the $\Delta^{33}S$ and $\Delta^{36}S$ co-variation (see Fig. S9 for sample 1308.08) and is instead more consistent with fractionations observed in cultures of sulfate reducers (*18*).

Modelling results for pyrite			
f	$\delta^{34}S$	$\Delta^{33}S$	$\Delta^{36}S$
1	-20.00	-3.17	2.72
0.95	-17.56	-3.15	2.63
0.9	-14.98	-3.14	2.54
0.85	-12.25	-3.13	2.44
0.8	-9.34	-3.11	2.34
0.75	-6.24	-3.10	2.22
0.7	-2.91	-3.08	2.10
0.65	0.68	-3.07	1.96
0.6	4.58	-3.05	1.81
0.55	8.83	-3.03	1.65
0.5	13.50	-3.00	1.47
0.45	18.70	-2.98	1.26

Open vs. closed system MSR

The greater ^{34}S depletion in the micro-scale analyses compared to bulk measurements suggests mass-dependent redistribution of sulfur isotopes by MSR in the

sediment. However, the negative $\delta^{34}S$ pyrite values (-10‰) preserved in bulk samples relative to the inferred positive $\delta^{34}S$ composition of coeval seawater SO_4^{2-} imply that the system is not completely closed. To evaluate the degree of closure in the sedimentary system during the formation of pyrite in the Batatal carbonates, we evaluated both batch and Rayleigh distillation processes. Using the Rayleigh equation (see above) and assuming $\alpha = 1.050$ (a maximal spread in $\delta^{34}S$ between seawater sulfate and pyrite in the Batatal Formation carbonates) and $R_0 = 1.015$ [assuming the initial sulfate composition $\delta^{34}S$ =+15‰ (*23*)]. Given these constraints, we estimate that the fraction of sulfate reduced during MSR is 0.5 and ~0.7 for batch and Rayleigh distillation processes, respectively, suggesting a partially closed system.

	Batch distillation		Rayleigh distillation	
f	$\delta^{34}S$(py)	$\delta^{34}S$(sulf)	$\delta^{34}S$(sulf)	$\delta^{34}S$(py)
1.0	-35	15	15.00	-
0.9	-30	20	20.36	-33.25
0.8	-25	25	26.39	-30.55
0.7	-20	30	33.26	-27.62
0.6	-15	35	41.26	-24.39
0.5	**-10**	40	50.79	-20.79
0.4	-5	45	62.58	-16.72
0.3	0	50	77.98	***-11.99***
0.2	5	55	100.06	-6.26
0.1	10	60	138.85	1.24
0.0	15	65	-	-

Closure of the Archean sulfur cycle?

With our discovery of carbonate associated pyrite with consistently negative $\Delta^{33}S$ signatures in the Batatal Formation coupled with previous results (*23, 31)* one might consider whether certain carbonate facies might represent a "hidden" reservoir for negative $\Delta^{33}S$. This consideration is important insofar as most of the Archean sulfur isotope measurements come from black shale, a fine-grained and often pyritic siliciclastic rock typically formed in distal settings with higher organic carbon contents. To evaluate the potential sink for negative $\Delta^{33}S$ in Neoarchean carbonates we use the mass balance equation:

$$\Delta^{33}S_{total} \cdot S_{total}\, N_{total} = \Delta^{33}S_{shale} \cdot N_{shale} \cdot S_{shale} + \Delta^{33}S_{carb} \cdot N_{carb} \cdot S_{carb},$$

where $\Delta^{33}S$ is the average composition of the Neoarchean total, shale, and carbonate sinks ($\Delta^{33}S_{total}$ should be zero to account for mass balance), S is an average sulfur content in total, shale, and carbonate sinks, and N is the total volume of sulfur in each Neoarchean sink (in this analysis we assume that there are only two sinks, shale and carbonate, although we recognize that there were most likely others). According to (*33*), in the Neoarchean the carbonate to shale ratio is about 2.2 to 1. Thus, we can estimate the

proportion of the sink possible through carbonate accumulation alone (with the caveat that not all Neoarchean carbonates preserve negative $\Delta^{33}S$ signatures).

Given the very low pyrite abundance in the Batatal carbonates (0.02±0.02%) with its average $\Delta^{33}S$ value (ca. -1.7‰) and the significantly higher concentration in co-eval shale (e.g. Mt.McRae Shale Formation, *20*; 2.92±2.77%) with its average $\Delta^{33}S$ value (+2.7‰), mass balance could be achieved if 80x more carbonate accumulated than is presently preserved in the Neoarchean geological record. In conclusion, the carbonate sink appears to represent only about 1% of the negative $\Delta^{33}S$ reservoir, so we must consider alternative chemical sinks in the oceanic realm.

Constraints of Neoarchean sulfate levels

The negative excursion in $\Delta^{33}S$ between core depths of 1302 to 1308 m may be used to constraint response time of sulfate. With the carbonate accumulation rates 40-150 m/10^6 yr (*29*), six meters would accumulate between 40,000 and 150,000 years. Fitting a first order kinetics box model to the data by solving for the evolution of each isotope independently using:

$$^{3i}S = \frac{^{3i}F_{input}}{k} - \left(\frac{^{3i}F_{input}}{k} - {}^{3i}S_{t=0}\right) e^{-kt}.$$

The fit is illustrated in Fig.S10. We calculate a residence time estimate between 20,000 and 75,000 yrs. The residence time equation,

$\tau = V/\phi$,

can be used to estimate the concentration of sulfate in the Neoarchean ocean, where τ is the residence time, V is the size of reservoir, and ϕ is the flux. For the Neoarchean we assume that the sulfur flux to the surface environment was primarily through volcanic emissions, which are estimated at ~ 10^{11} mol/yr. The calculated mass of the sulfate reservoir is thus in the range of 10^{15} to 10^{16} moles. If we assume that the ancient ocean had the same mass as today ($1.4 \cdot 10^{21}$ kg), the sulfate concentration would have been in the range of 1 to 10 μMol/L.

Carbon isotope fractionation

Mineralogical differences between shale and carbonate environments suggest variable carbon and sulfur abundance as well as isotopic composition across the Batatal basin and also a pronounced change in each parameter with depth. Siderite, the dominant carbonate mineral in basinal iron-formation and off shore shale of the Neoarchean, is typically depleted in ^{13}C by 5 to 7‰, relative to massive coeval dolomite and limestone deposits forming in shallow marine environments (*41*). This may be explained if deep water alkalinity (and CO_2) mixed slowly with the shallow ocean and evolved to lower ^{13}C abundances through anaerobic respiratory processes (*21, 42*), including MSR. Paragenetic and carbon isotopic studies of BIF carbonates (*43*, *44*) suggest that chert, siderite, and the iron-silicate greenalite were most likely primary precipitates forming in the water column or along the sediment water interface. This observation is consistent with the isotopic homogeneity of siderite microbands (as opposed to bands that are

replaced by rhombic ankerite or magnetite), as well as the long-range correlation of bands at macroscopic and microscopic scales. Alternatively, the ^{13}C depletion in siderite with banded iron-formation or shale might reflect microbial oxidation of organic matter (likely using Fe^{3+} or SO_4^{2-}) and production of authigenic carbonate within the sediment (*21*, *42*).

In contrast, shallow ocean alkalinity would be largely sourced from the weathering of exposed continental rocks; dissolved CO_2 used by photoautotrophs in shallow near shore environments would be in equilibrium with the atmosphere. This is reflected in the near 0‰ values of samples from the carbonate member of the Batatal Formation and shallow marine carbonate platforms of Neoarchean age worldwide. On the other hand, the overall ^{13}C relative enrichment in organic matter and notably reduced fractionation of carbon isotopes revealed in the Batatal carbonate samples suggests CO_2 limitation (*45*). The partial pressure of CO_2 in seawater is controlled by temperature, salinity, and evaporation, as well as its rate of autotrophic uptake (*46*), which can all affect the magnitude of carbon isotope fractionation. Ultimately low concentrations of ambient CO_2 or high rates of autotrophic growth result in ^{13}C enrichment of organic matter as carbon fixation rates outpace those of diffusion. Carbon dioxide limitation in modern evaporitic settings, such as those represented by Shark Bay in Western Australia (*47*), the Bahamas (*48*) and sabkhas in the Middle East (*49*) results in significant ^{13}C enrichment of dissolved and particulate organic matter, with $\delta^{13}C_{org}$ values ranging from -20 up to -5‰. Insofar as silica is concentrated by evaporation of seawater, the widespread occurrence of chert cement in the Batatal carbonate samples is consistent with shallow marine conditions associated with higher temperatures and evaporation (Fig. S4). Notably, many reactions involved in microbial sulfate reduction are known to increase the acidity of pore waters, which promote the dissolution of carbonate and the crystallization of chert.

Whether formed in the water column or in sediments, the organic source of alkalinity for siderite would result in ^{13}C depletion and reduced magnitude of carbon isotope fractionation in deep water shale or banded iron-formation facies. Furthermore, in distal shale facies the source of organic matter must have been distinct from that of proximal carbonates (based on their carbon isotope contrast), most likely related to planktonic as opposed to benthic inputs. This explanation, however, does not address the 10-15‰ enrichment of ^{13}C in organic matter in the Brazilian shale facies in comparison to similar co-eval, but deeper, environments in Western Australia and South Africa (Fig. S11). Given the metamorphic grade of the Brazilian succession as lower greenschist (*37*), the ^{13}C enrichment of the organic fraction is not likely the result of thermal effects (*50*) while average organic carbon contents in the Brazilian black shale samples are low relative to those in the equivalent deep water examples where the significant depletion in ^{13}C is consistent with chemolithotrophic or methanotrophic inputs to the sediments (*51*).

The overall mineralogical, elemental, and isotopic differences between facies may reflect shallow-to-deep gradients in oxygen, alkalinity, and dissolved organic carbon. It seems likely that deep basinal water was ferruginous while dissolved hydrogen sulfide was able to build up in pore fluids through MSR where it would complex with ferrous iron to form insoluble pyrite. Hydrogen sulfide concentrations may have also risen in shallow water carbonate pore fluids, but pyrite formation may have been limited by a general lack of ferrous iron and source of reductants to fuel the microbial process. Other potential causes for iron limitation in the shallow marine environment may be related to photo-oxidation, oxidation by free oxygen, or microbial uptake. Combined these

processes are likely the reason why pyrite concentrations are so low in the Batatal Formation carbonates.

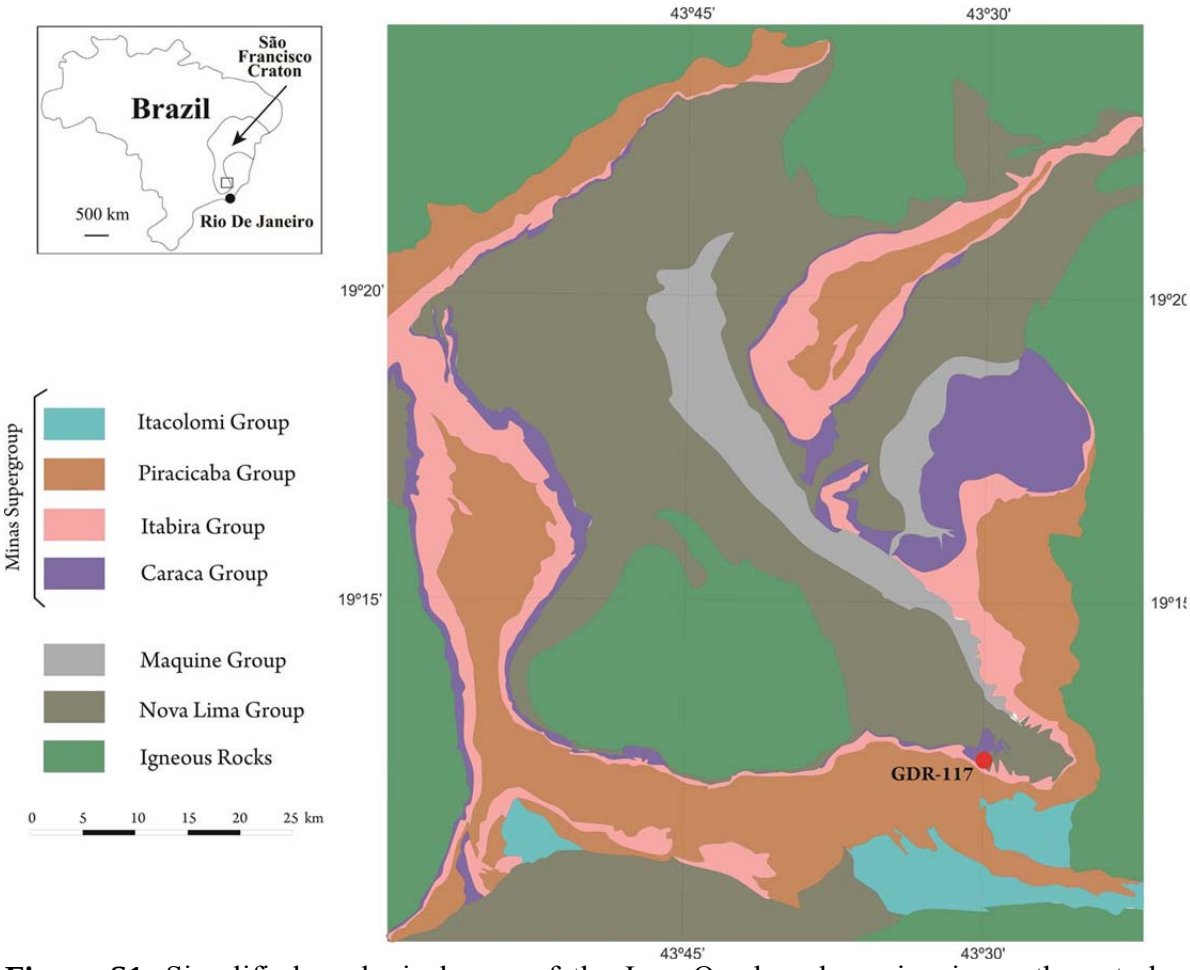

Figure S1. Simplified geological map of the Iron Quadrangle region in south-central Brazil with the position of the GDR-117 core (after *38*).

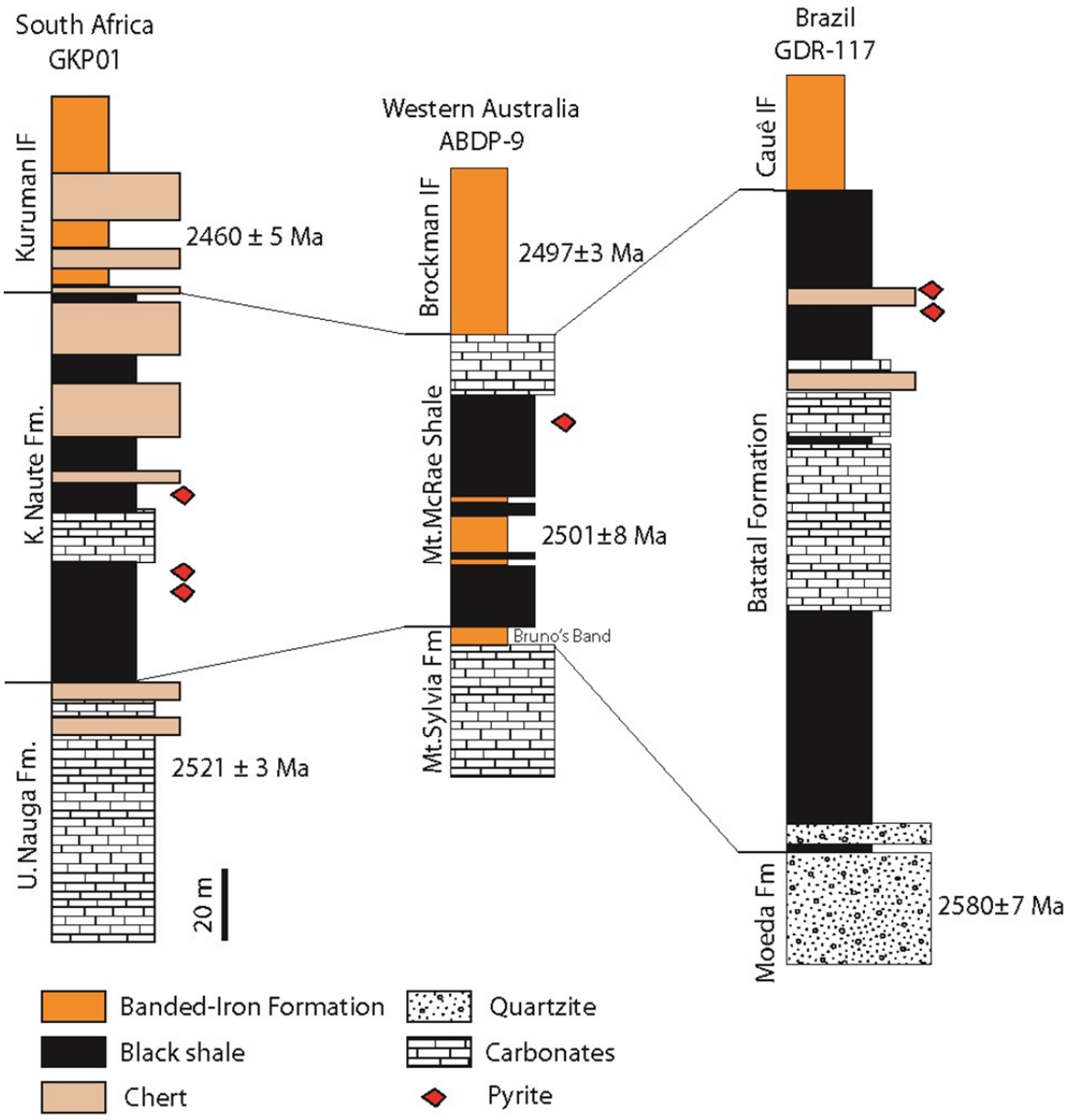

Figure S2: Simplified stratigraphic columns of cores GKP01 (South Africa), ABDP-9 (Western Australia), and GDR-117 (Brazil) drawn at equivalent scale. Age constraints are from reference *34, 52-55*. Scale did not allow to include the Gandarela Fm. with the age of 2.42 Ga (Pb-Pb, *35*), an upper constraint for the Batatal Fm. The lithological transitions and pyrite enrichments are common in all three successions. Lithology is from references *20, 22, and 38*.

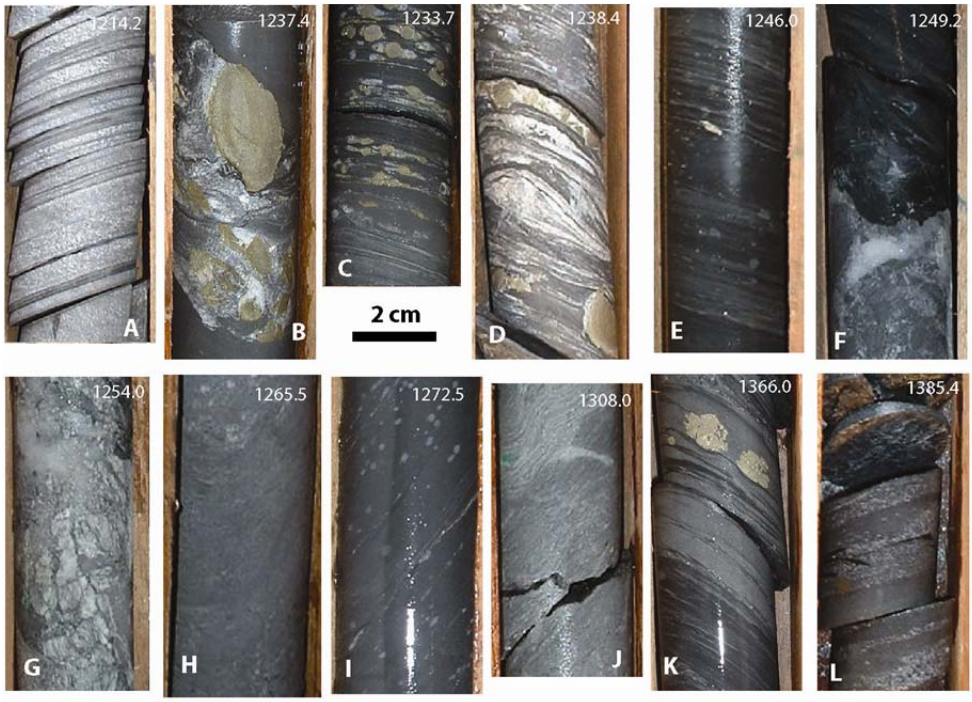

Figure S3. Lithological variability of the Batatal Formation. A, B, C, D, E – upper black shale with an interval enriched in pyrite. F – a karst contact between quartz-carbonate breccia and upper shale. G, H, I, J – examples of carbonate facies with laminations and some tracers of stromatolites. K, L – lower black to grey shale.

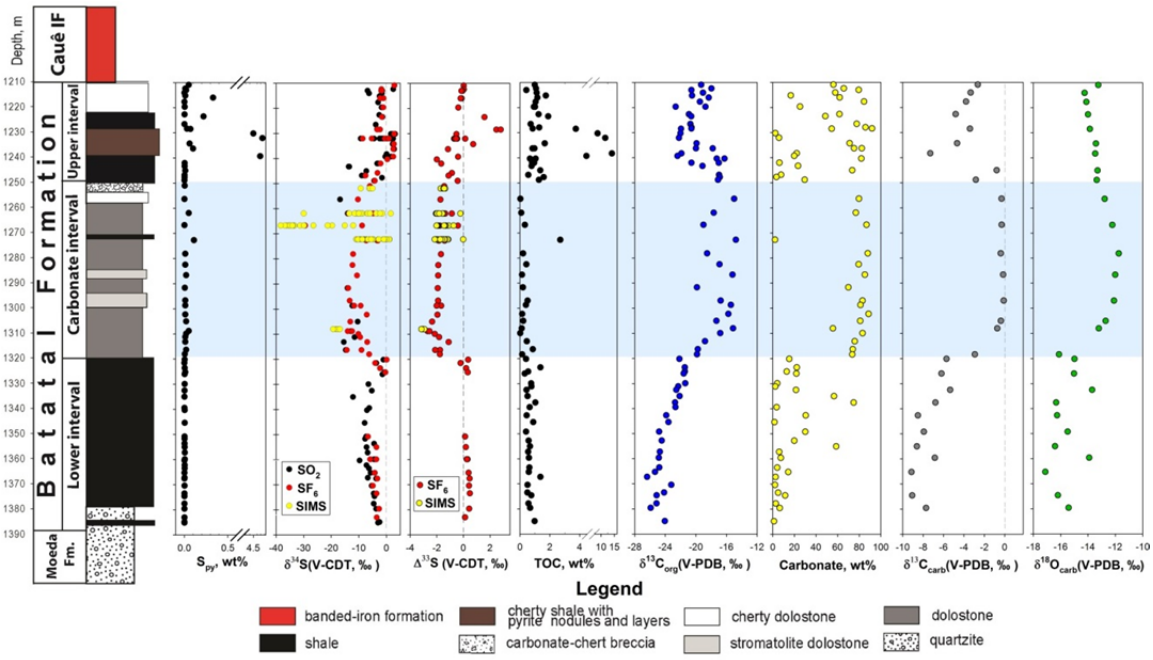

Figure S4. Time-series sulfur and carbon concentrations, as well as sulfur, carbon, and oxygen isotope abundances of samples of the Batatal Formation from the GDR-117 core in south-central Brazil.

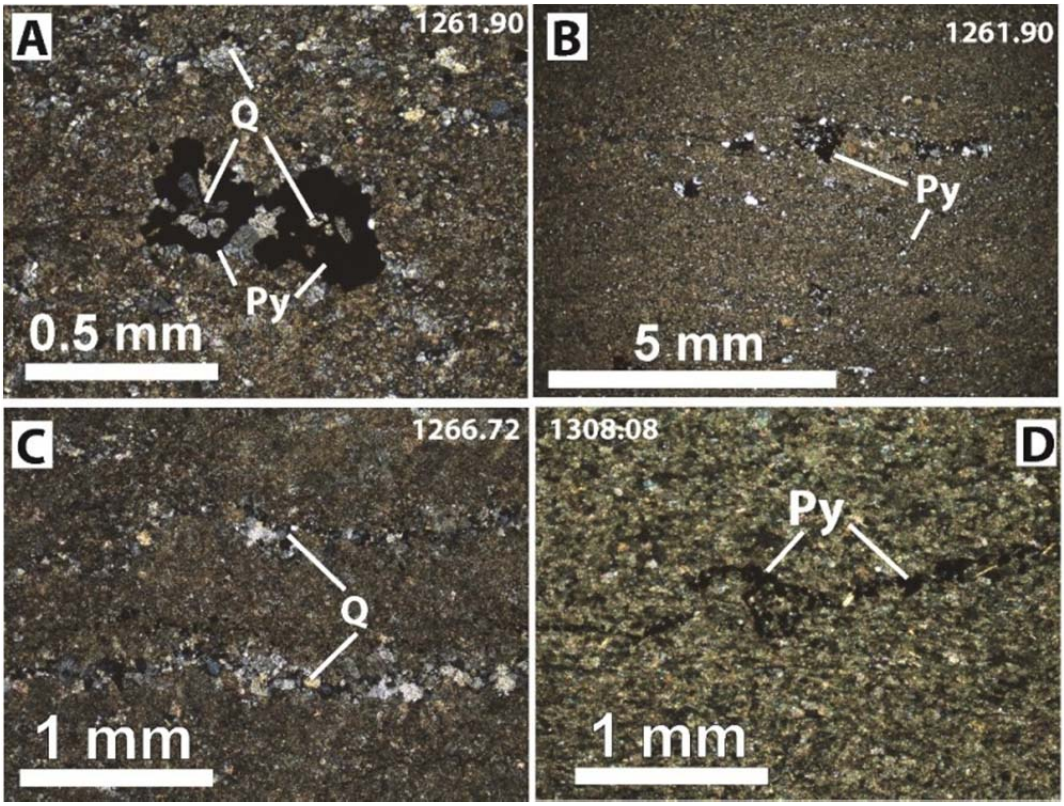

Figure S5. Microphotographs of thin sections from carbonate interval of the Batatal Formation. Q and Py are quartz and pyrite, respectively. Crossed nicol.

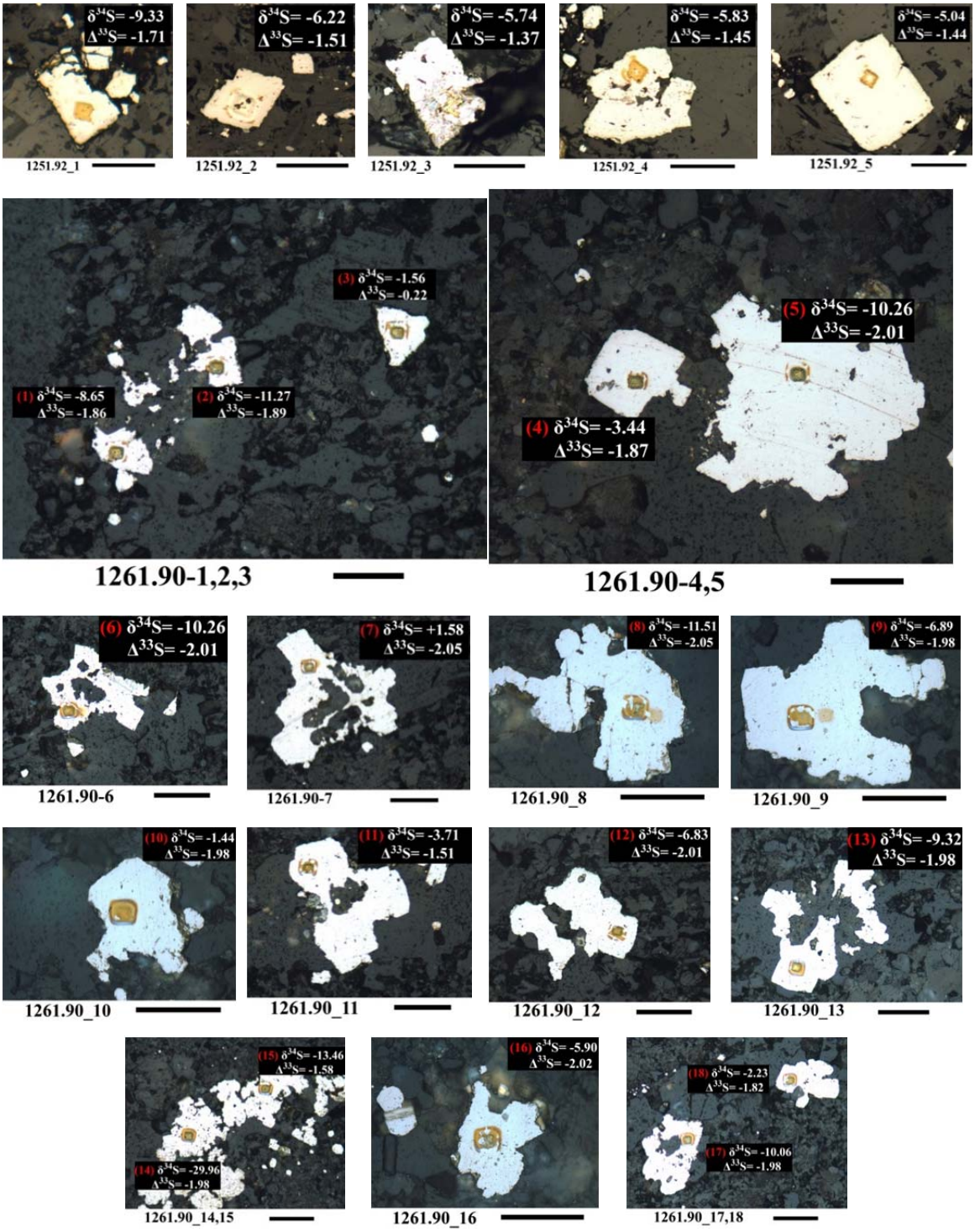

Figure S6a. Microphotographs of pyrite grains in carbonate associated pyrite from samples at 1251.92 and 1261.90 m depth showing SIMS isotopic measurements. Small yellow squares are SIMS pits and include a ~ 30 μm × 30 μm pre-sputter area followed by a smaller ~25 μm × 25 μm analysis area.

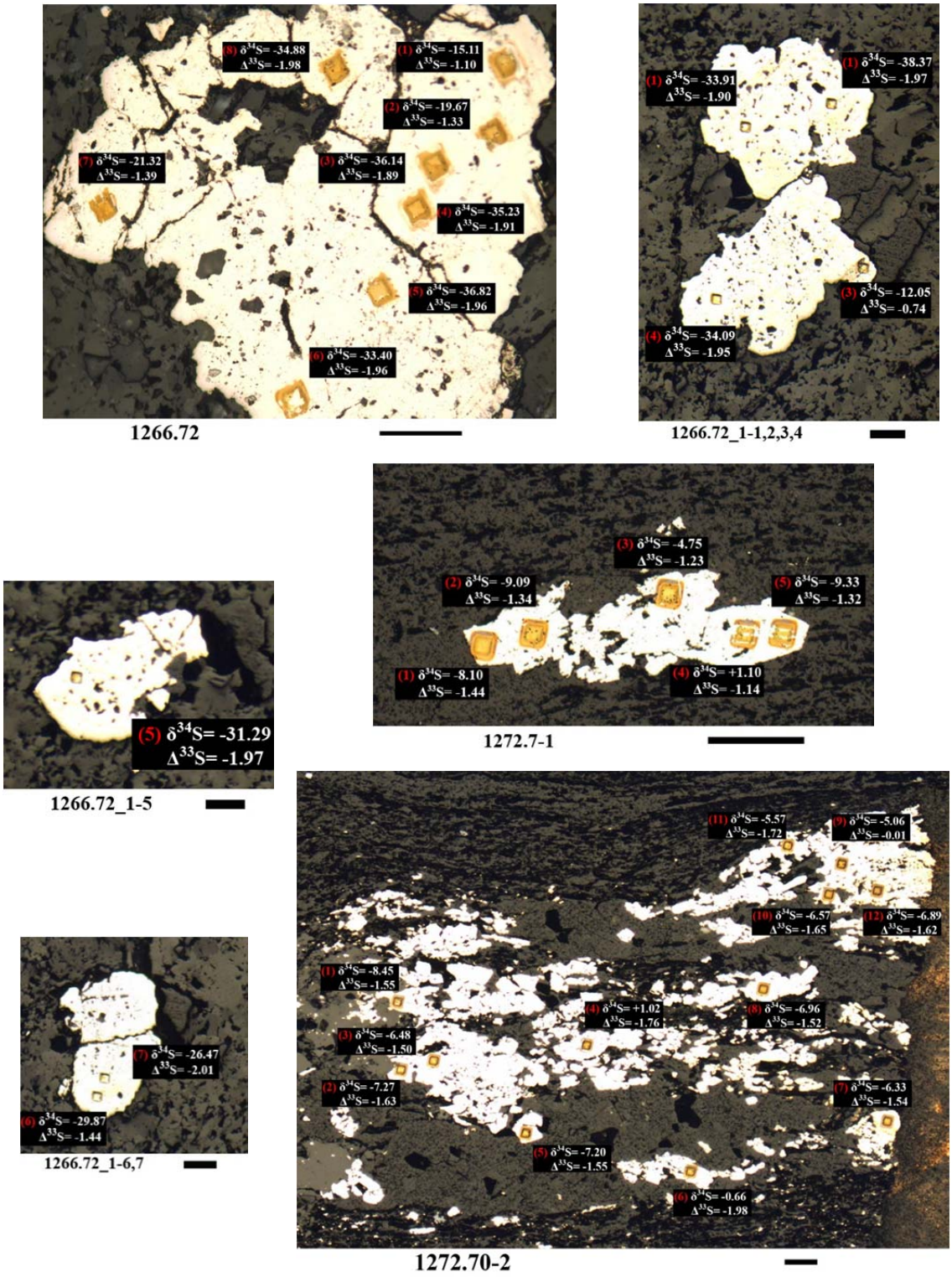

Figure S6b. Microphotographs of pyrite grains in carbonate associated pyrite from samples at 1266.72 and 1270.70 (1, 2) m depth showing SIMS isotopic measurements. Small yellow squares are SIMS pits and include a ~ 30 μm × 30 μm pre-sputter area followed by a smaller ~25 μm × 25 μm analysis area.

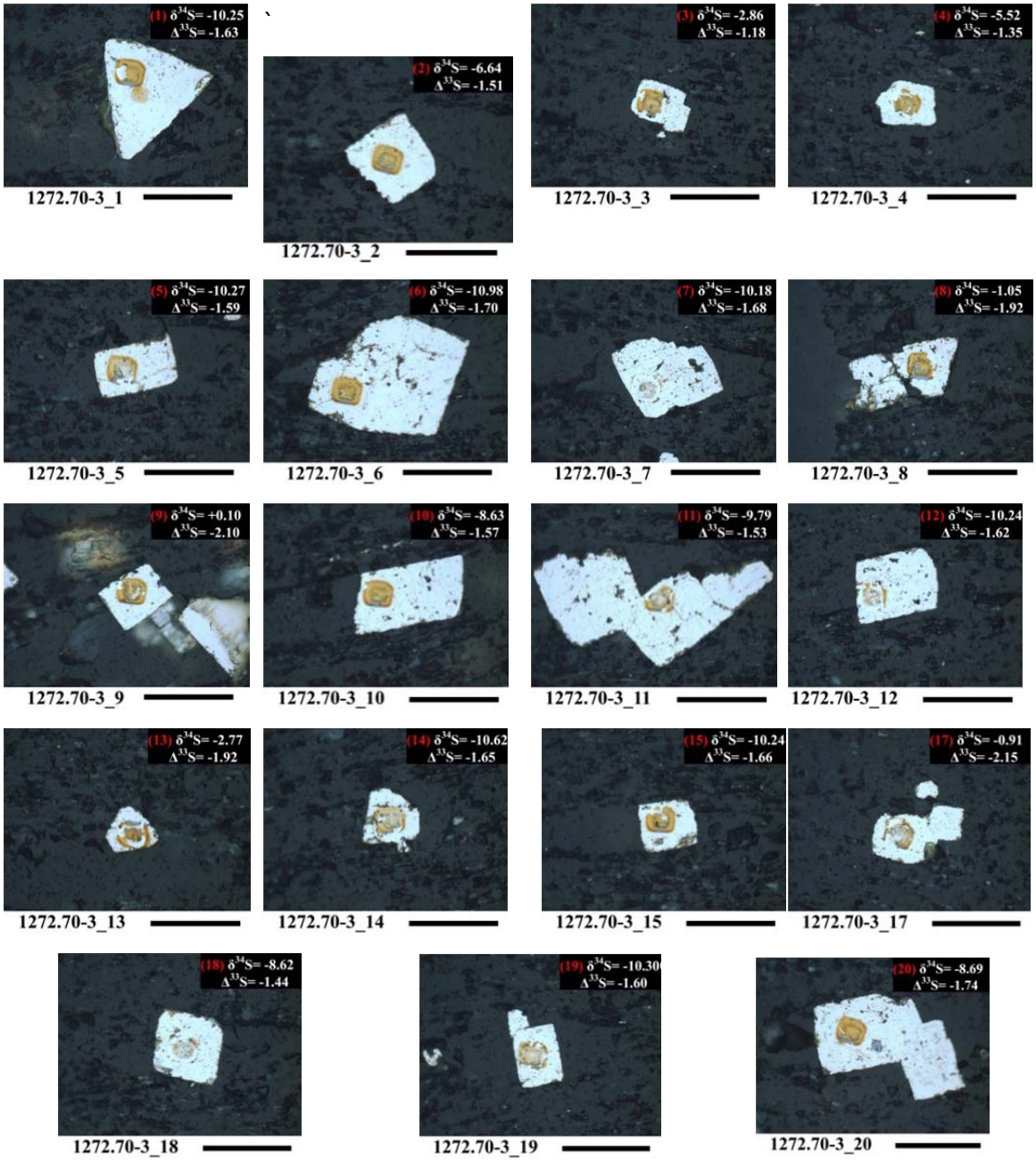

Figure S6c. Microphotographs of pyrite grains in carbonate associated pyrite from samples at 1270.70 (3) m depth showing SIMS isotopic measurements. Small yellow squares are SIMS pits and include a ~ 30 μm × 30 μm pre-sputter area followed by a smaller ~25 μm × 25 μm analysis area.

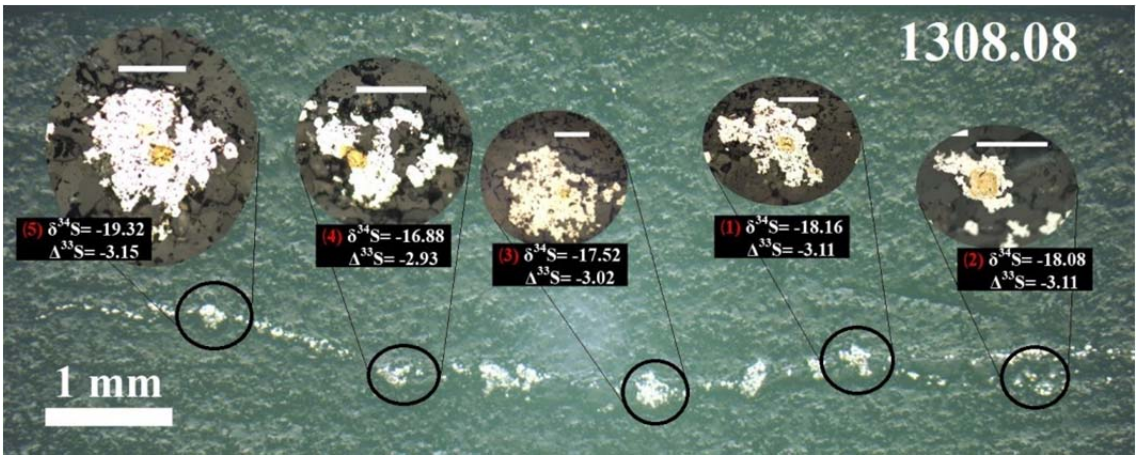

Figure S6d. Microphotographs of pyrite grains in carbonate associated pyrite from samples at 1308.08 m depth showing SIMS isotopic measurements. Small yellow squares are SIMS pits and include a ~ 30 μm × 30 μm pre-sputter area followed by a smaller ~25 μm × 25 μm analysis area.

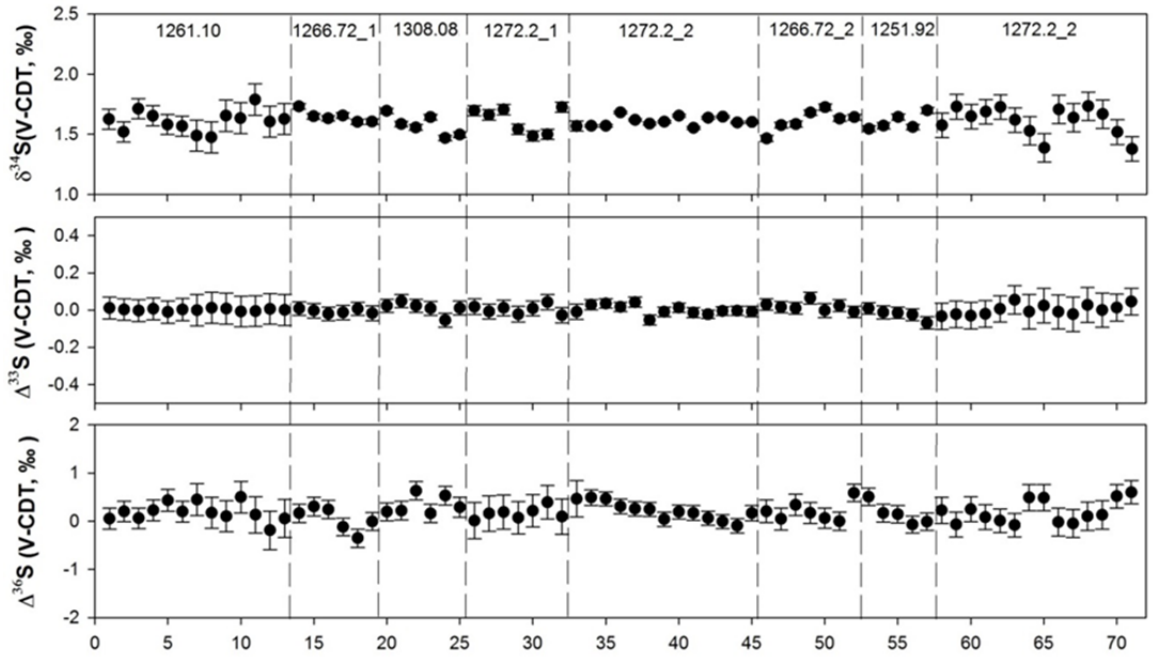

Figure S7. Variations of isotopic composition $\delta^{34}S$, $\Delta^{33}S$ and $\Delta^{36}S$ for standard SON-3 throughout the measurement process using SIMS. Dashed lines separate values of bracketing standards between samples (samples name can be seen at the top of the figure).

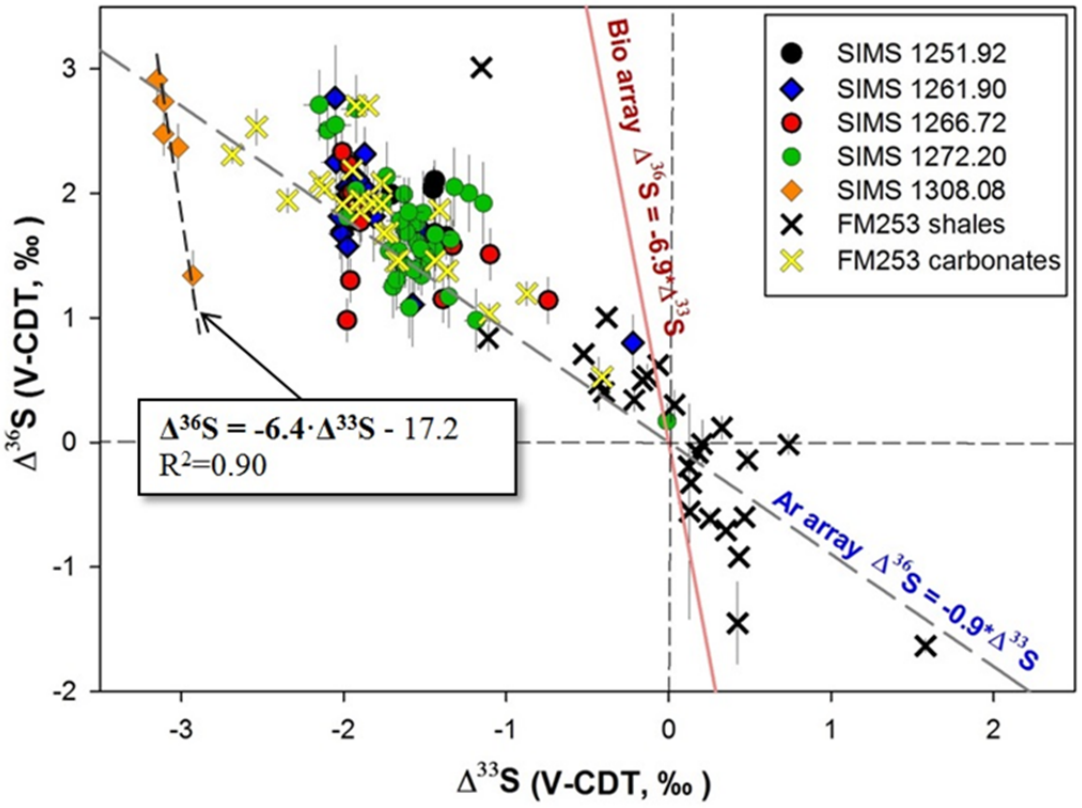

Figure S8. Cross-plot $\Delta^{36}S$ vs. $\Delta^{33}S$ for Batatal pyrites from bulk/drilled and SIMS analyses. Relative to the slope Some SIMS analyses show enrichment or depletion in ^{36}S relative to Archean array (*5*). Sample 1308.08 where pyrite laminas were measured (Fig. S5) exhibits $\Delta^{36}S/\Delta^{33}S$ slope -6.4 (R^2=0.90) similar to observed biological Phanerozoic signatures (19) where $\Delta^{36}S/\Delta^{33}S$~-6.9 caused by Rayleigh distillation (see SOM text and Fig. S11). However, sample 1308.08 most likely preserved mass-dependent biological signatures (*18*) overprinting MIF (negative $\Delta^{33}S$) caused by atmospheric reactions in the absence of an ozone shield (*5*).

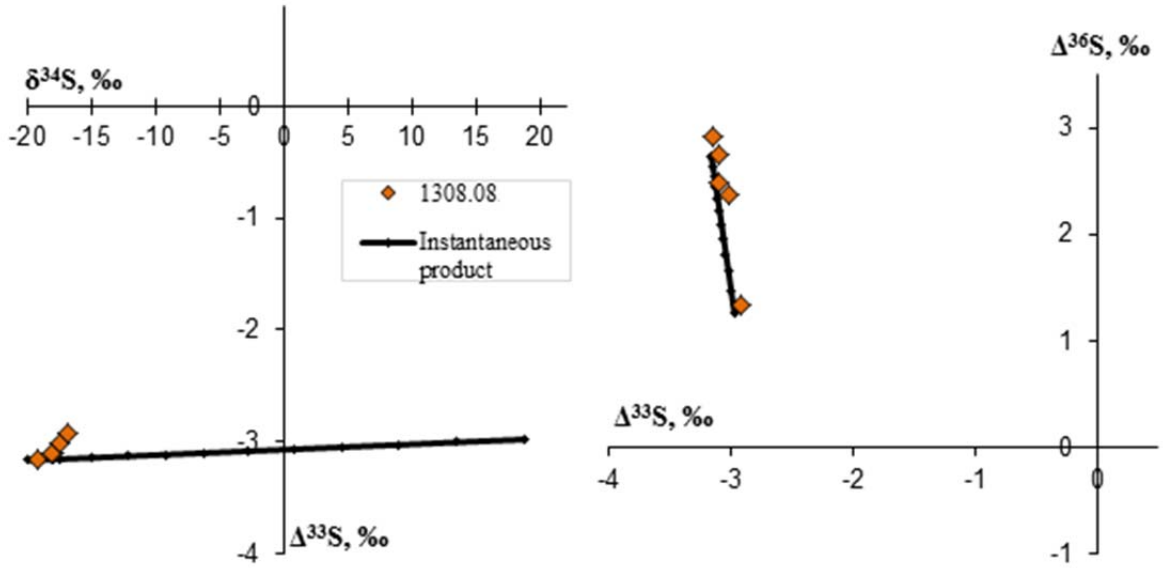

Figure S9. Modelling of instantanious product during Rayleigh distillation for the sample 1308.08

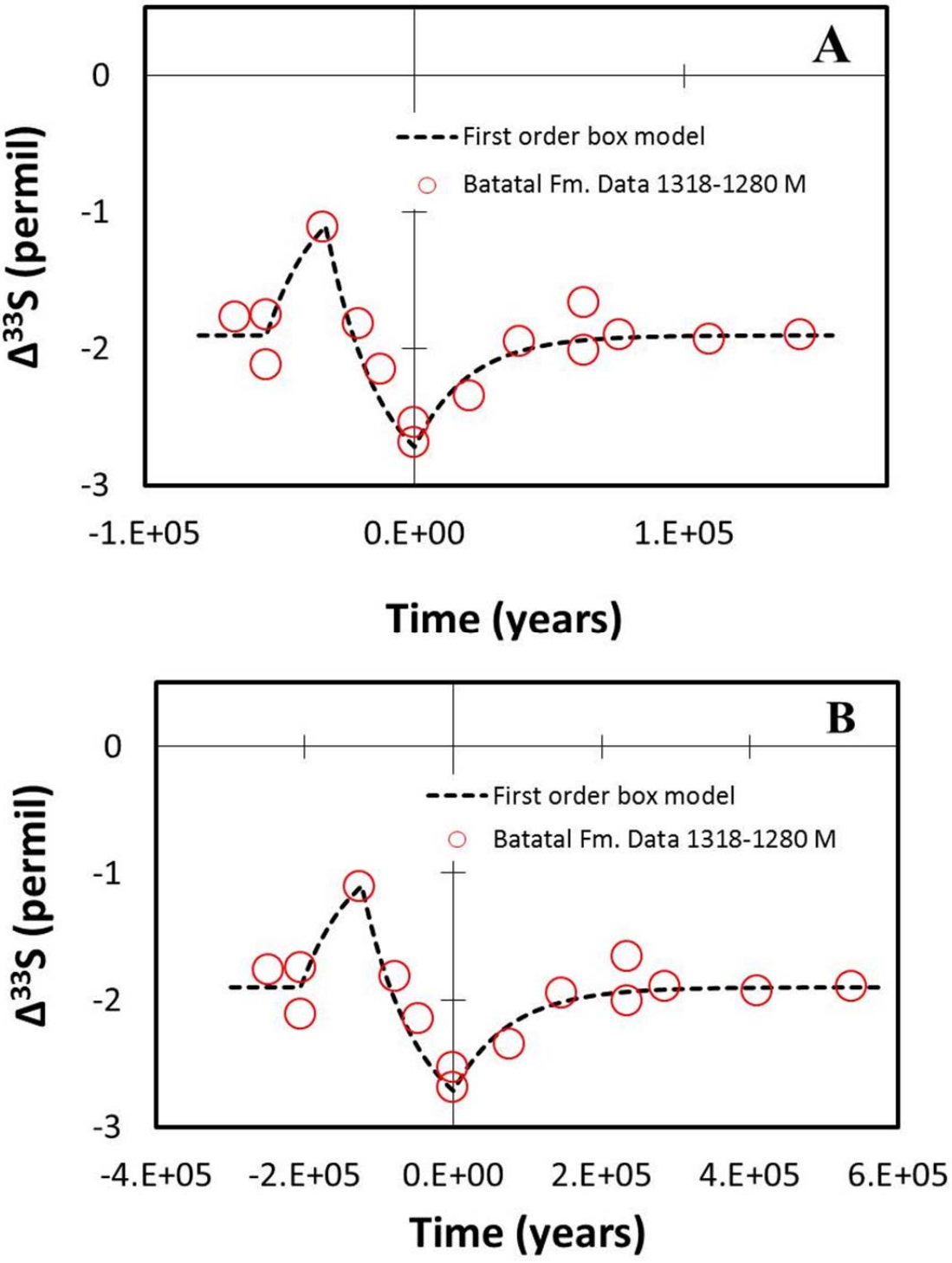

Figure S10. Plot of first order kinetic box model $\Delta^{33}S$ evolution versus time. A. calculation assuming 6 meters accumulates in 40,000 yrs. B. calculation assuming 6 meters accumulates in 150,000 yrs.

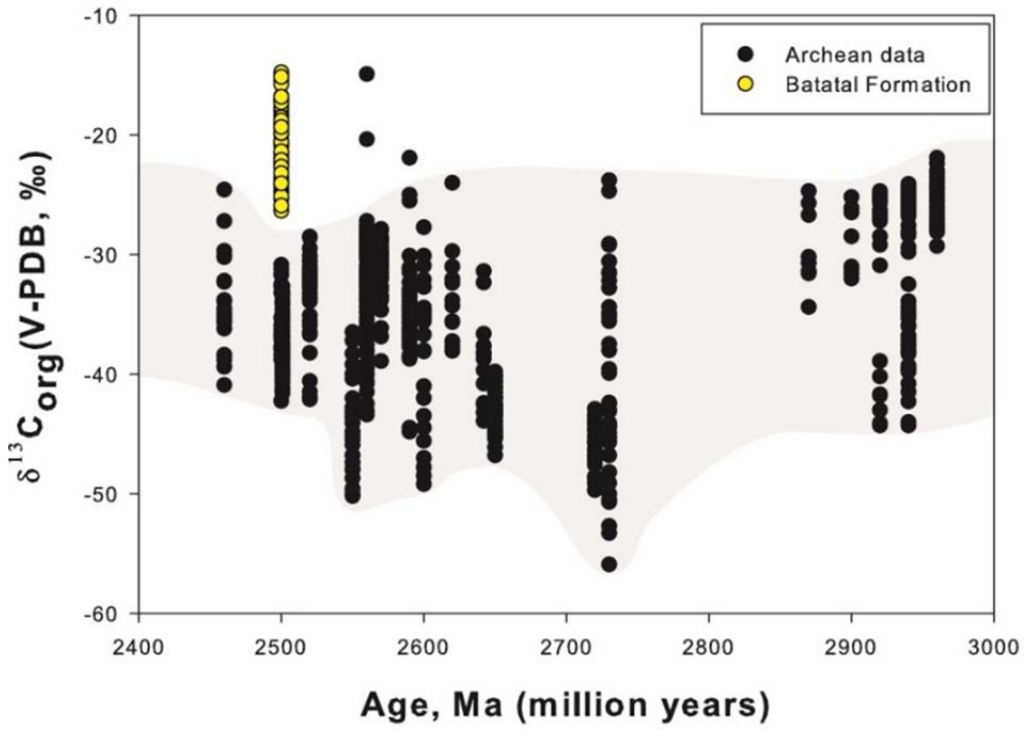

Figure S11. Carbon isotopic composition of organic matter from Archean successions and ca. 2.5 Ga Batatal Formation. Data are from *20, 21, 51, 56, 57*

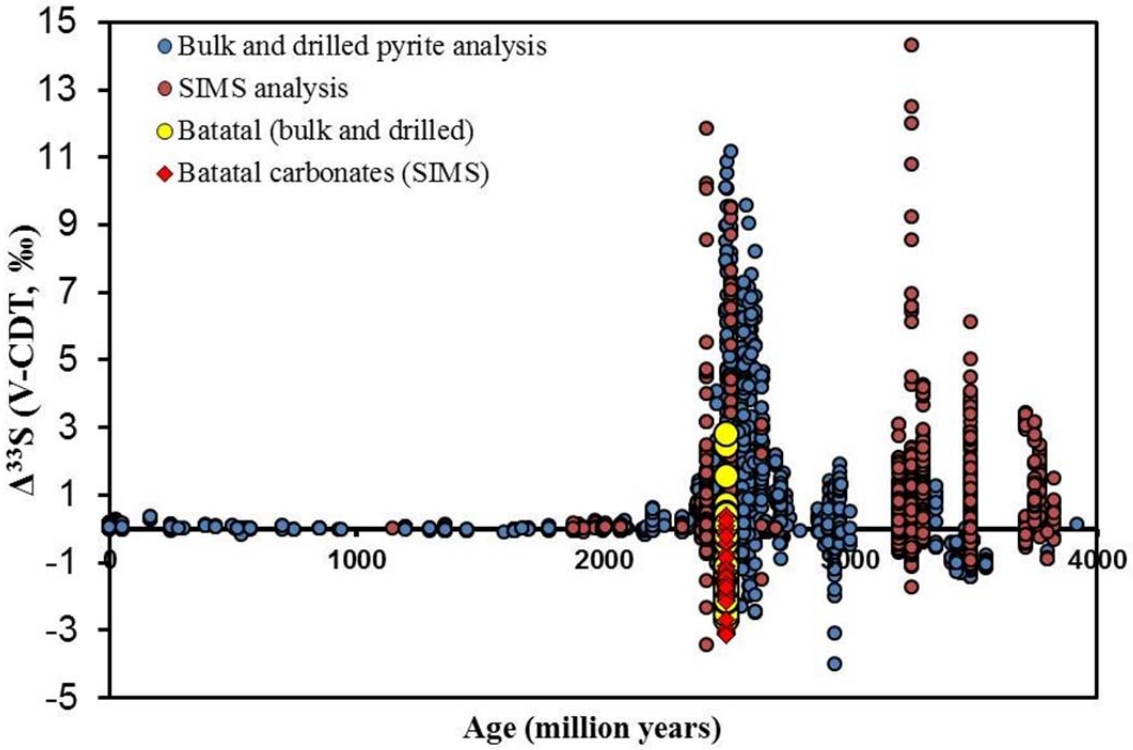

Figure S12. Plot of $\Delta^{33}S$ variation over geological timescale. SIMS analyses are separated from bulk/drilled pyrite. Compiled data are from *7, 12, 58-72*.

Additiional Data
Tables S1 and S2 (separate file **zhelezinskaia_TablesS1_S2.xlsx**)

Table S1. Sulfur, carbon and oxygen isotope data of the Batatal Formation, Brazil. SO_2 – measurement by Elemental Analyzer-IRMS Isoprime, SF_6 – measurements by Thermo Finnigan MAT 253, "py" is noted for drilled pyrite.

Table S2. SIMS analysis of five samples from the Batatal carbonate interval

References and Notes

1. A. A. Pavlov, J. F. Kasting, Mass-independent fractionation of sulfur isotopes in Archean sediments: Strong evidence for an anoxic Archean atmosphere. *Astrobiology* **2**, 27–41 (2002). Medline doi:10.1089/153110702753621321

2. K. S. Habicht, M. Gade, B. Thamdrup, P. Berg, D. E. Canfield, Calibration of sulfate levels in the archean ocean. *Science* **298**, 2372–2374 (2002). Medline doi:10.1126/science.1078265

3. J. W. Jamieson, B. A. Wing, J. Farquhar, M. D. Hannington, Neoarchaean seawater sulphate concentrations from sulphur isotopes in massive sulphide ore. *Nat. Geosci.* **6**, 61–64 (2013). doi:10.1038/ngeo1647

4. Y. Shen, J. Farquhar, A. Masterson, A. J. Kaufman, R. Buick, Evaluating the role of microbial sulfate reduction in the early Archean using quadruple isotope systematics. *Earth Planet. Sci. Lett.* **279**, 383–391 (2009). doi:10.1016/j.epsl.2009.01.018

5. J. Farquhar, J. Savarino, S. Airieau, M. H. Thiemens, Observation of wavelength-sensitive mass-independent sulfur isotope effects during SO_2 photolysis: Implications for the early atmosphere. *J. Geophys. Res.* **106**, 32829–32839 (2001). doi:10.1029/2000JE001437

6. D. E. Canfield, The evolution of the Earth surface sulfur reservoir. *Am. J. Sci.* **304**, 839–861 (2004). doi:10.2475/ajs.304.10.839

7. D. T. Johnston, Multiple sulfur isotopes and the evolution of Earth's surface sulfur cycle. *Earth Sci. Rev.* **106**, 161–183 (2011). doi:10.1016/j.earscirev.2011.02.003

8. I. Halevy, D. T. Johnston, D. P. Schrag, Explaining the structure of the Archean mass-independent sulfur isotope record. *Science* **329**, 204–207 (2010). Medline doi:10.1126/science.1190298

9. C. T. Reinhard, N. J. Planavsky, T. W. Lyons, Long-term sedimentary recycling of rare sulphur isotope anomalies. *Nature* **497**, 100–103 (2013). Medline doi:10.1038/nature12021

10. C. T. Reinhard, R. Raiswell, C. Scott, A. D. Anbar, T. W. Lyons, A late Archean sulfidic sea stimulated by early oxidative weathering of the continents. *Science* **326**, 713–716 (2009). Medline doi:10.1126/science.1176711

11. B. S. Kamber, M. J. Whitehouse, Micro-scale sulphur isotope evidence for sulphur cycling in the late Archean shallow ocean. *Geobiology* **5**, 5–17 (2007). doi:10.1111/j.1472-4669.2006.00091.x

12. J. Farquhar, J. Cliff, A. L. Zerkle, A. Kamyshny, S. W. Poulton, M. Claire, D. Adams, B. Harms, Pathways for Neoarchean pyrite formation constrained by mass-independent sulfur isotopes. *Proc. Natl. Acad. Sci. U.S.A.* **110**, 17638–17643 (2013). Medline doi:10.1073/pnas.1218851110

13. D. Wacey, M. R. Kilburn, M. Saunders, J. Cliff, M. D. Brasier, Microfossils of sulphur-metabolizing cells in 3.4-billion-year-old rocks of Western Australia. *Nat. Geosci.* **4**, 698–702 (2011). doi:10.1038/ngeo1238

14. T. R. Bontognali, A. L. Sessions, A. C. Allwood, W. W. Fischer, J. P. Grotzinger, R. E. Summons, J. M. Eiler, Sulfur isotopes of organic matter preserved in 3.45-billion-year-old stromatolites reveal microbial metabolism. *Proc. Natl. Acad. Sci. U.S.A.* **109**, 15146–15151 (2012). Medline doi:10.1073/pnas.1207491109

15. See supplementary materials on *Science* Online.

16. E. S. Cheney, Sequence stratigraphy and plate tectonic significance of the Transvaal succession of southern Africa and its equivalent in Western Australia. *Precambrian Res.* **79**, 3–24 (1996). doi:10.1016/0301-9268(95)00085-2

17. Sulfur has four stable isotopes: two more abundant (^{32}S and ^{34}S) and two rare (^{33}S and ^{36}S) isotopes. Sulfur isotope composition of materials is reported as $\delta^{x}S = 1000 \times [(^{x}S/^{32}S)_{sample}/(^{x}S/^{32}S)_{standard} - 1]$, where x is 33, 34, or 36.

18. The deviation from the mass-dependent relationships is calculated by the following equations: $\Delta^{33}S = \delta^{33}S - 1000 \times [(\delta^{34}S/1000 + 1)^{0.515} - 1]$ and $\Delta^{36}S = \delta^{36}S - 1000 \times [(\delta^{34}S/1000 + 1)^{1.90} - 1]$.

19. D. T. Johnston, J. Farquhar, D. E. Canfield, Sulfur isotope insights into microbial sulfate reduction: When microbes meet models. *Geochim. Cosmochim. Acta* **71**, 3929–3947 (2007). doi:10.1016/j.gca.2007.05.008

20. S. Ono, B. Wing, D. Johnston, J. Farquhar, D. Rumble, Mass-dependent fractionation of quadruple stable sulfur isotope system as a new tracer of sulfur biogeochemical cycles. *Geochim. Cosmochim. Acta* **70**, 2238–2252 (2006). doi:10.1016/j.gca.2006.01.022

21. A. J. Kaufman, D. T. Johnston, J. Farquhar, A. L. Masterson, T. W. Lyons, S. Bates, A. D. Anbar, G. L. Arnold, J. Garvin, R. Buick, Late Archean biospheric oxygenation and atmospheric evolution. *Science* **317**, 1900–1903 (2007). Medline doi:10.1126/science.1138700

22. W. W. Fischer, S. Schroeder, J. P. Lacassie, N. J. Beukes, T. Goldberg, H. Strauss, U. E. Horstmann, D. P. Schrag, A. H. Knoll, Isotopic constraints on the Late Archean carbon cycle from the Transvaal Supergroup along the western margin of the Kaapvaal Craton, South Africa. *Precambrian Res.* **169**, 15–27 (2009). doi:10.1016/j.precamres.2008.10.010

23. S. Ono, A. J. Kaufman, J. Farquhar, D. Y. Sumner, N. J. Beukes, Lithofacies control on multiple-sulfur isotope records and Neoarchean sulfur cycles. *Precambrian Res.* **169**, 58–67 (2009). doi:10.1016/j.precamres.2008.10.013

24. S. Ono, J. L. Eigenbrode, A. A. Pavlov, P. Kharecha, D. Rumble III, J. F. Kasting, K. H. Freeman, New insights into Archean sulfur cycle from mass-independent sulfur isotope records from the Hamersley Basin, Australia. *Earth Planet. Sci. Lett.* **213**, 15–30 (2003). doi:10.1016/S0012-821X(03)00295-4

25. G. Paris, J. F. Adkins, A. L. Sessions, S. A. Crowe, C. Jones, D. A. Fowle, D. E. Canfield, Profile of sulfate isotopic composition of Lake Matano, Indonesia. *Mineral. Mag.* **76**, 2204 (2012).

26. M. L. Gomes, M. T. Hurtgen, Sulfur isotope systematics of a euxinic, low-sulfate lake: Evaluating the importance of the reservoir effect in modern and ancient oceans. *Geology* **41**, 663–666 (2013). doi:10.1130/G34187.1

27. W. D. Leavitt, I. Halevy, A. S. Bradley, D. T. Johnston, Influence of sulfate reduction rates on the Phanerozoic sulfur isotope record. *Proc. Natl. Acad. Sci. U.S.A.* **110**, 11244–11249 (2013). Medline doi:10.1073/pnas.1218874110

28. I. Halevy, Production, preservation, and biological processing of mass-independent sulfur isotope fractionation in the Archean surface environment. *Proc. Natl. Acad. Sci. U.S.A.* **110**, 17644–17649 (2013). Medline doi:10.1073/pnas.1213148110

29. W. Altermann, D. R. Nelson, Sedimentation rates, basin analysis and regional correlations of three Neoarchaean and Palaeoproterozoic sub-basins of the Kaapvaal craton as inferred from precise U-Pb zircon ages from volcaniclastic sediments. *Sediment. Geol.* **120**, 225–256 (1998). doi:10.1016/S0037-0738(98)00034-7

30. J. Farquhar, B. A. Wing, Multiple sulfur isotopes and the evolution of the atmosphere. *Earth Planet. Sci. Lett.* **213**, 1–13 (2003). doi:10.1016/S0012-821X(03)00296-6

31. M. A. Partridge, S. D. Golding, K. A. Baublys, E. Young, Pyrite paragenesis and multiple sulfur isotope distribution in late Archean and early Paleoproterozoic Hamersley Basin sediments. *Earth Planet. Sci. Lett.* **272**, 41–49 (2008). doi:10.1016/j.epsl.2008.03.051

32. B. M. Simonson, K. A. Schubel, S. W. Hassler, Carbonate sedimentology of the early Precambrian Hamersley Group of Western Australia. *Precambrian Res.* **60**, 287–335 (1993). doi:10.1016/0301-9268(93)90052-4

33. K. C. Condie, D. J. Des Marais, D. Abbott, Precambrian superplumes and supercontinents: A record in black shales, carbon isotopes, and paleoclimates? *Precambrian Res.* **106**, 239–260 (2001). doi:10.1016/S0301-9268(00)00097-8

34. L. A. Hartmann, I. Endo, M. T. F. Suita, J. O. S. Santos, J. C. Frantz, M. A. Carneiro, N. J. McNaughton, M. E. Barley, Provenance and age delimitation of Quadrilátero Ferrífero sandstones based on zircon U-Pb isotopes. *J. S. Am. Earth Sci.* **20**, 273–285 (2006). doi:10.1016/j.jsames.2005.07.015

35. M. Babinski, F. Chemale Jr., W. R. Van Schmus, The Pb-Pb age of the Minas Supergroup carbonate rocks, Quadrilátero Ferrífero, Brazil. *Precambrian Res.* **72**, 235–245 (1995). doi:10.1016/0301-9268(94)00091-5

36. S. Marshak, S. F. F. Alkmim, Proterozoic contraction/extension tectonics of the southern São Francisco region, Minas Gerais, Brazil. *Tectonics* **8**, 555–571 (1989). doi:10.1029/TC008i003p00555

37. N. Herz, *Metamorphic Rocks of the Quadrilátero Ferrífero, Minas Gerais, Brazil: A Study of the Metamorphic Events that Have Affected the Precambrian Igneous and Metasedimentary Rocks of the Brazilian Shield* (U.S. Government Printing Office, 1978).

38. J. Dorr, *Physiographic, Stratigraphic and Structural Development of the Quadrilátero Ferrífero, Minas Gerais, Brazil* (USGS Prof. Pap., 1969).

39. N. J. Beukes, C. Klein, A. J. Kaufman, J. M. Hayes, Carbonate petrography, kerogen distribution, and carbon and oxygen isotope variations in an early Proterozoic transition from limestone to iron-formation deposition, Transvaal Supergroup, South Africa. *Econ. Geol.* **85**, 663–690 (1990). Medline doi:10.2113/gsecongeo.85.4.663

40. D. P. Schrag, J. A. Higgins, F. A. Macdonald, D. T. Johnston, Authigenic carbonate and the history of the global carbon cycle. *Science* **339**, 540–543 (2013). Medline doi:10.1126/science.1229578

41. A. J. Kaufman, J. M. Hayes, C. Klein, Primary and diagenetic controls of isotopic compositions of iron-formation carbonates. *Geochim. Cosmochim. Acta* **54**, 3461–3473 (1990). Medline doi:10.1016/0016-7037(90)90298-Y

42. B. L. Winter, L. P. Knauth, Stable isotope geochemistry of cherts and carbonates from the 2.0 Ga Gunflint Iron Formation: Implications for the depositional setting, and the effects of diagenesis and metamorphism. *Precambrian Res.* **59**, 283–313 (1992). doi:10.1016/0301-9268(92)90061-R

43. E. A. Laws, R. R. Bidigare, B. N. Popp, Effect of growth rate and CO_2 concentration on carbon isotopic fractionation by the marine diatom *Phaeodactylum tricornutum*. *Limnol. Oceanogr.* **42**, 1552–1560 (1997). doi:10.4319/lo.1997.42.7.1552

44. I. E. Woodrow, J. A. Berry, Enzymatic regulation of photosynthetic CO_2 fixation in C3 plants. *Annu. Rev. Plant Physiol. Plant Mol. Biol.* **39**, 533–594 (1988). doi:10.1146/annurev.pp.39.060188.002533

45. K. M. Cawley, Y. Ding, J. Fourqurean, R. Jaffé, Characterising the sources and fate of dissolved organic matter in Shark Bay, Australia: A preliminary study using optical properties and stable carbon isotopes. *Mar. Freshw. Res.* **63**, 1098–1107 (2012). doi:10.1071/MF12028

46. M. S. Andres, D. Y. Sumner, R. P. Reid, P. K. Swart, Isotopic fingerprints of microbial respiration in aragonite from Bahamian stromatolites. *Geology* **34**, 973–976 (2006). doi:10.1130/G22859A.1

47. M. Schidlowski, U. Matzigkeit, W. E. Krumbein, Superheavy organic carbon from hypersaline microbial mats. *Naturwissenschaften* **71**, 303–308 (1984). doi:10.1007/BF00396613

48. J. M. Hayes, I. R. Kaplan, K. M. Wedeking, in *Earth's Earliest Biosphere: Its Origin and Evolution*, J. W. Schopf, Ed. (Princeton Univ. Press, Princeton, NJ, 1983), pp. 93–135.

49. J. L. Eigenbrode, K. H. Freeman, Late Archean rise of aerobic microbial ecosystems. *Proc. Natl. Acad. Sci. U.S.A.* **103**, 15759–15764 (2006). Medline doi:10.1073/pnas.0607540103

50. C. Spötl, Long-term performance of the Gasbench isotope ratio mass spectrometry system for the stable isotope analysis of carbonate microsamples. *Rapid Commun. Mass Spectrom.* **25**, 1683–1685 (2011). Medline doi:10.1002/rcm.5037

51. T. B. Coplen, W. A. Brand, M. Gehre, M. Gröning, H. A. Meijer, B. Toman, R. M. Verkouteren, New guidelines for $\delta^{13}C$ measurements. *Anal. Chem.* **78**, 2439–2441 (2006). Medline doi:10.1021/ac052027c

52. A. L. Pickard, SHRIMP U-Pb zircon ages for the Palaeoproterozoic Kuruman Iron Formation, Northern Cape Province, South Africa: Evidence for simultaneous BIF deposition on Kaapvaal and Pilbara Cratons. *Precambrian Res.* **125**, 275–315 (2003). doi:10.1016/S0301-9268(03)00113-X

53. D. Y. Sumner, S. A. Bowring, U-Pb geochronologic constraints on deposition of the Campbellrand Subgroup, Transvaal Supergroup, South Africa. *Precambrian Res.* **79**, 25–35 (1996). doi:10.1016/0301-9268(95)00086-0

54. D. R. Nelson, A. F. Trendall, W. Altermann, Chronological correlations between the Pilbara and Kaapvaal cratons. *Precambrian Res.* **97**, 165–189 (1999). doi:10.1016/S0301-9268(99)00031-5

55. A. D. Anbar, Y. Duan, T. W. Lyons, G. L. Arnold, B. Kendall, R. A. Creaser, A. J. Kaufman, G. W. Gordon, C. Scott, J. Garvin, R. Buick, A whiff of oxygen before the great oxidation event? *Science* **317**, 1903–1906 (2007). Medline doi:10.1126/science.1140325

56. S. Ono, N. J. Beukes, D. Rumble, M. L. Fogel, Early evolution of atmospheric oxygen from multiple-sulfur and carbon isotope records of the 2.9 Ga Mozaan Group of the Pongola Supergroup, Southern Africa. *S. Afr. J. Geol.* **109**, 97–108 (2006). doi:10.2113/gssajg.109.1-2.97

57. C. Thomazo, M. Ader, J. Farquhar, P. Philippot, Methanotrophs regulated atmospheric sulfur isotope anomalies during the Mesoarchean (Tumbiana Formation, Western Australia). *Earth Planet. Sci. Lett.* **279**, 65–75 (2009). doi:10.1016/j.epsl.2008.12.036

58. B. Kendall, C. T. Reinhard, T. W. Lyons, A. J. Kaufman, S. W. Poulton, A. D. Anbar, Pervasive oxygenation along late Archaean ocean margins. *Nat. Geosci.* **3**, 647–652 (2010). doi:10.1038/ngeo942

59. B. M. Guy, S. Ono, J. Gutzmer, A. J. Kaufman, Y. Lin, M. L. Fogel, N. J. Beukes, A multiple sulfur and organic carbon isotope record from non-conglomeratic sedimentary rocks of the Mesoarchean Witwatersrand Supergroup, South Africa. *Precambrian Res.* **216–219**, 208–231 (2012). doi:10.1016/j.precamres.2012.06.018

60. A. L. Zerkle, M. W. Claire, S. D. Domagal-Goldman, J. Farquhar, S. W. Poulton, A bistable organic-rich atmosphere on the Neoarchaean Earth. *Nat. Geosci.* **5**, 359–363 (2012). doi:10.1038/ngeo1425

61. K. Scheiderich, A. L. Zerkle, G. R. Helz, J. Farquhar, R. J. Walker, Molybdenum isotope, multiple sulfur isotope, and redox-sensitive element behavior in early Pleistocene Mediterranean sapropels. *Chem. Geol.* **279**, 134–144 (2010). doi:10.1016/j.chemgeo.2010.10.015

62. N. Wu, J. Farquhar, H. Strauss, S. T. Kim, D. E. Canfield, Evaluating the S-isotope fractionation associated with Phanerozoic pyrite burial. *Geochim. Cosmochim. Acta* **74**, 2053–2071 (2010). doi:10.1016/j.gca.2009.12.012

63. S. Fabre, A. Nédélec, F. Poitrasson, H. Strauss, C. Thomazo, A. Nogueira, Iron and sulphur isotopes from the Carajás mining province (Pará, Brazil): Implications for the oxidation of the ocean and the atmosphere across the Archaean-Proterozoic transition. *Chem. Geol.* **289**, 124–139 (2011). doi:10.1016/j.chemgeo.2011.07.019

64. S. D. Golding *et al*., in *Earliest Life on Earth: Habitats, Environments and Methods of Detection*, S. D. Golding, M. Glikson, Eds. (Springer, New York, 2011), pp. 15–49.

65. Y. Shen, J. Farquhar, H. Zhang, A. Masterson, T. Zhang, B. A. Wing, Multiple S-isotopic evidence for episodic shoaling of anoxic water during Late Permian mass extinction. *Nat. Commun.* **2**, 210 (2011). Medline doi:10.1038/ncomms1217

66. K. H. Williford, M. J. Van Kranendonk, T. Ushikubo, R. Kozdon, J. W. Valley, Constraining atmospheric oxygen and seawater sulfate concentrations during Paleoproterozoic glaciation: In situ sulfur three-isotope microanalysis of pyrite from the Turee Creek Group, Western Australia. *Geochim. Cosmochim. Acta* **75**, 5686–5705 (2011). doi:10.1016/j.gca.2011.07.010

67. B. Bühn, R. V. Santos, M. A. Dardenne, C. G. de Oliveira, Mass-dependent and mass-independent sulfur isotope fractionation ($\delta^{34}S$ and $\delta^{33}S$) from Brazilian Archean and Proterozoic sulfide deposits by laser ablation multi-collector ICP-MS. *Chem. Geol.* **312**, 163–176 (2012). doi:10.1016/j.chemgeo.2012.04.003

68. M. L. Fiorentini, A. Bekker, O. Rouxel, B. A. Wing, W. Maier, D. Rumble, Multiple sulfur and iron isotope composition of magmatic Ni-Cu-(PGE) sulfide mineralization from eastern Botswana. *Econ. Geol.* **107**, 105–116 (2012). doi:10.2113/econgeo.107.1.105

69. P. Philippot, M. van Zuilen, C. Rollion-Bard, Variations in atmospheric sulphur chemistry on early Earth linked to volcanic activity. *Nat. Geosci*. **5**, 668–674 (2012). doi:10.1038/ngeo1534

70. D. L. Roerdink, P. R. Mason, J. Farquhar, T. Reimer, Multiple sulfur isotopes in Paleoarchean barites identify an important role for microbial sulfate reduction in the early

marine environment. *Earth Planet. Sci. Lett.* **331**, 177–186 (2012). doi:10.1016/j.epsl.2012.03.020

71. F. Kurzweil, M. Claire, C. Thomazo, M. Peters, M. Hannington, H. Strauss, Atmospheric sulfur rearrangement 2.7 billion years ago: Evidence for oxygenic photosynthesis. *Earth Planet. Sci. Lett.* **366**, 17–26 (2013). doi:10.1016/j.epsl.2013.01.028

72. D. L. Roerdink, P. R. Mason, M. J. Whitehouse, T. Reimer, High-resolution quadruple sulfur isotope analyses of 3.2 Ga pyrite from the Barberton Greenstone Belt in South Africa reveal distinct environmental controls on sulfide isotopic arrays. *Geochim. Cosmochim. Acta* **117**, 203–215 (2013). doi:10.1016/j.gca.2013.04.027